ADVANCING EARTH AND SPACE SCIENCES

Geochemistry, Geophysics, Geosystems

RESEARCH ARTICLE
10.1029/2025GC012823

Special Collection:
Slow to fast earthquakes and the geology, structure, and rheology of their host subduction zones

Key Points:

- We impose periodic pore-pressure perturbations on mildly velocity-weakening faults to examine the resulting slow-slip event (SSE) behaviors
- Our model shows that periodic pore-pressure changes induce SSEs, earthquakes, and mixed behaviors
- Realistic SSEs may form more readily on velocity-strengthening than on velocity-weakening faults under pore-pressure perturbations

Supporting Information:

Supporting Information may be found in the online version of this article.

Correspondence to:

A. Perez-Silva,
acperez@gfz.de

Citation:

Perez-Silva, A., Kaneko, Y., & Wang, T. (2026). Pore-pressure cycles and slow slip generation on mildly velocity-weakening faults. *Geochemistry, Geophysics, Geosystems*, *27*, e2025GC012823. https://doi.org/10.1029/2025GC012823

Received 20 NOV 2025
Accepted 8 JUN 2026

Author Contributions:

Conceptualization: Andrea Perez-Silva, Yoshihiro Kaneko, Ting Wang
Data curation: Andrea Perez-Silva
Formal analysis: Andrea Perez-Silva
Funding acquisition: Ting Wang
Investigation: Andrea Perez-Silva
Methodology: Andrea Perez-Silva, Yoshihiro Kaneko

Pore-Pressure Cycles and Slow Slip Generation on Mildly Velocity-Weakening Faults

Andrea Perez-Silva[1,2], Yoshihiro Kaneko[3], and Ting Wang[1]

[1]University of Otago, Dunedin, New Zealand, [2]Now at GFZ Helmholtz Centre for Geosciences, Potsdam, Germany, [3]Department of Geophysics, Graduate School of Science, Kyoto University, Kyoto, Japan

Abstract Recent observations have revealed pore-fluid pressure fluctuations correlated with the occurrence of slow slip events (SSEs) in several subduction zones. These fluctuations, caused by fluid accumulation and migration before and during SSEs, may modulate the timing and characteristics of these events. To test whether pore-pressure changes can induce SSEs comparable to observations, we develop a physical model in which periodic changes in pore-fluid pressure are imposed on a planar velocity-weakening fault by varying the effective normal stress (one-way coupling). Fluid is assumed to be injected at the center of the fault and to diffuse along the fault plane according to the axisymmetric diffusion equation. Our results show that these perturbations produce a spectrum of slip behaviors, from quasi-periodic SSEs to earthquakes, including mixed behaviors. The induced SSEs have durations and magnitudes ranging from approximately 3 months to over a year and M_w5.5–7.5. However, the model does not reproduce the full range of SSE properties observed in subduction zones, and the parameter space leading to SSEs is narrower than that of models with velocity-strengthening faults. These findings support the previously proposed idea that SSEs are more consistently reproduced by models of velocity-strengthening faults than by models of velocity-weakening faults subjected to pore-pressure perturbations.

Plain Language Summary Slow slip events are a type of fault movement that occurs much more slowly than regular earthquakes and can last for weeks or months instead of seconds. These slow events are thought to be influenced by changes in the pressure of fluids moving through tiny spaces in rocks deep underground. When fluid pressure changes, it can affect how easily rocks slip past each other. To better understand this process, we developed a computer model of a fault in which fluid is repeatedly injected at the center and then spreads over time. Using this model, we tested whether changes in fluid pressure, combined with different frictional properties of the fault, can trigger slow slip events similar to those observed in nature. We found that models with certain frictional properties better reproduce the characteristics of these events. We also found that, for the model to match real-world slow slip events, the fault zone must allow fluids to pass through easily.

1. Introduction

Recent observations have inferred pore-fluid pressure fluctuations that correlate with the occurrence of slow slip events (SSEs) in subduction zones, such as Cascadia (Gosselin et al., 2020), Hikurangi (Herath & Audet, 2024; Warren-Smith et al., 2019; Zal et al., 2020), Nankai (Kita et al., 2021), Sagami (Nakajima & Uchida, 2018), and Mexico (Frank et al., 2015). Such fluctuations have been inferred based on changes in seismic velocity, relative principal stresses, seismic anisotropy, seismic attenuation, and changes in the acceleration rate of low frequency earthquakes during SSEs. A compelling example of these pore-pressure cycles occurred along the Hikurangi subduction zone, which marks the subduction of the Pacific plate beneath the Australian plate. Here, Warren-Smith et al. (2019) uncovered systematic changes in the relative magnitude of principal compressive stresses that temporally correlate with shallow SSEs. These changes, used as a proxy for pore-fluid pressure, uncovered a pattern in which pore-fluid pressure increases during the inter-SSE period and decreases at the onset of slip.

The inferred pore-pressure cycles have been interpreted in the context of the fault valve model (Sibson, 1992). In this model, episodes of fluid accumulation and drainage are driven by permeability changes along the plate interface. Before SSEs, fault zone permeability is low (Audet et al., 2009; Peacock et al., 2011), which traps fluids within the subducting slab, thus increasing pore-fluid pressure. As pore-pressure builds up, it eventually reaches a near-lithostatic value, which breaks the low-permeability seal and induces slip at the plate interface. The onset of

Project administration: Ting Wang
Software: Yoshihiro Kaneko
Validation: Andrea Perez-Silva
Visualization: Andrea Perez-Silva
Writing – original draft: Andrea Perez-Silva
Writing – review & editing: Andrea Perez-Silva, Yoshihiro Kaneko, Ting Wang

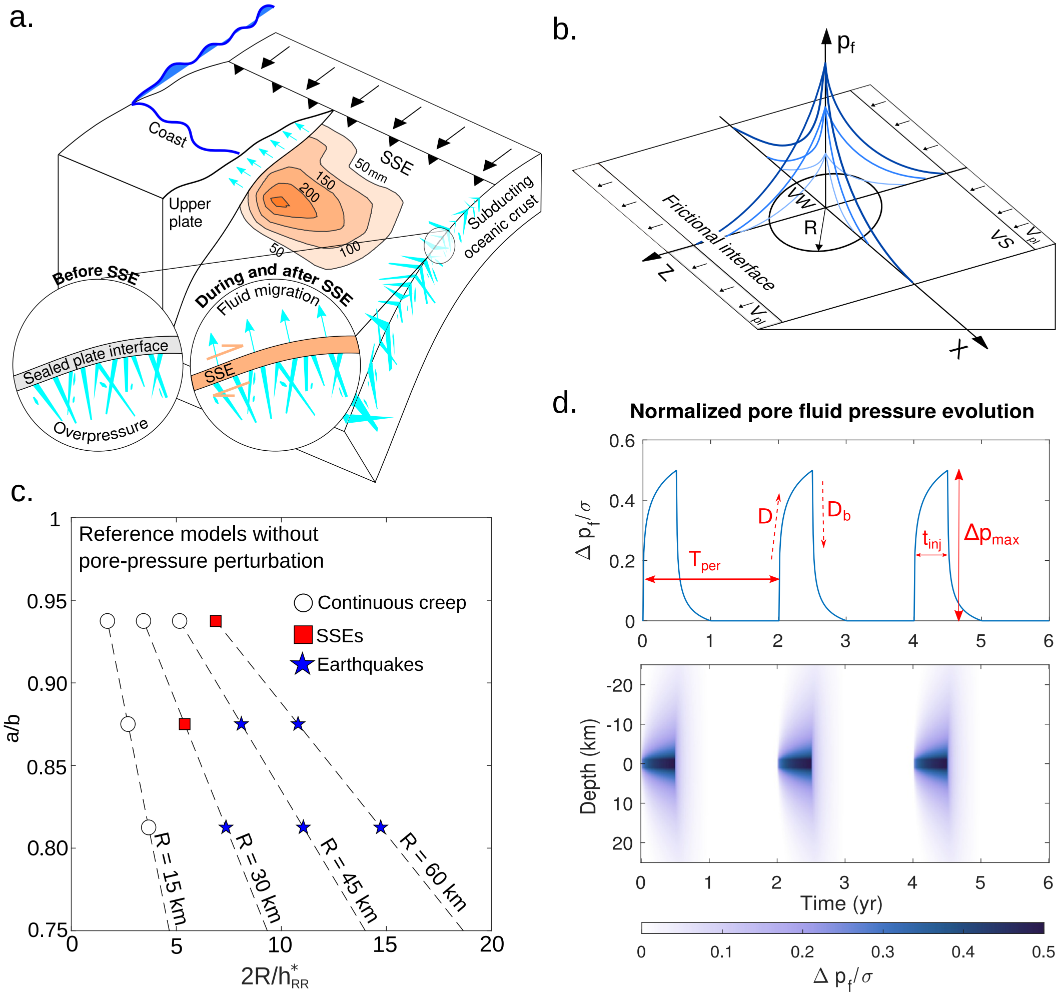

Figure 1. (a) Schematic diagram showing a conceptual model of pore-pressure cycling during shallow Hikurangi SSEs, based on Warren-Smith et al. (2019). Orange contours show cumulative slip during the 2016 shallow Gisborne SSE (Wallace et al., 2016). Thick cyan lines indicate fractures. (b) Schematic of our model setup showing a pore-pressure increase at the fault center (blue lines with different shades indicate consecutive time steps) and the properties of the frictional interface, where VW stands for velocity-weakening and VS for velocity-strengthening. R is the radius of the VW patch. (c) Exploration of model parameters a/b and $2R/h^*_{RR}$ for simulation cases without pore-pressure perturbations. Fault response is classified into continuous creep (white circles), SSEs ($V < 10^{-2}$ m/s, red squares) and earthquakes ($V > 10^{-2}$ m/s, blue stars). (d) Example of modeled pore fluid pressure changes assuming axis-symmetric fluid diffusion. Temporal change in normalized pore fluid pressure is shown at the fault center (top) and along z (bottom). Perturbation parameters are explained in Section 2 and Text S2 in Supporting Information S1.

slip generates fractures, which allow upward fluid flow and decrease pore-fluid pressure. The cycle continues as mineral precipitation closes the fractures thus decreasing permeability (Warren-Smith, et al., 2019). A schematic diagram of this process is shown in Figure 1a. This interpretation is supported by field observations showing crack-seal veins indicating large-scale fluid circulation (Behr & Bürgmann, 2021; Condit & French, 2022; Muñoz-Montecinos & Behr, 2023; Oncken et al., 2022).

Observations of pore-pressure fluctuations during SSEs have challenged our understanding of their physical mechanisms. Early numerical models of SSEs within the rate-and-state friction framework (RSF, Dieterich, 1979; Marone, 1998) typically assumed constant pore-fluid pressure, velocity-weakening friction and relied on alternative processes (e.g., transition to rate-strengthening friction at higher slip speeds, Shibazaki & Iio, 2003; dilatancy strengthening, Segall et al., 2010; transitional friction behavior, Liu & Rice, 2007) as stabilizing mechanisms. More recent models have explored the role of fluids more explicitly, coupling fluid flow and fault slip to account for the evolution of permeability, porosity, pore-pressure and slip (e.g., Ozawa et al., 2024; Yang &

Dunham, 2023; Zhu et al., 2020). Given that these models account for two-way coupling of fluid flow and fault slip, computational costs are intensive and geometry is typically restricted to 2-D, which limits comparison to observations. Other models have examined the generation of pore-pressure waves (Cruz-Atienza et al., 2018), the effect of fluid pressure diffusion on a frictionally heterogeneous fault (Hosseini et al., 2025), the evolution of pore-pressure and permeability (e.g., Farge et al., 2021), or have studied fluid flow in pore-elastic (e.g., Heimisson et al., 2019; Marguin & Simpson, 2023) or visco-elastic rheologies (e.g., Zilio & Gerya, 2022). Despite these advances, the extent to which pore-pressure changes along faults can initiate or modulate SSEs remains an open question.

An alternative modeling approach by Perez-Silva et al. (2023) explored the effects of pore-pressure changes on fault slip by imposing variations in effective normal stress (i.e., one-way coupling). They found that periodic pore-pressure fluctuations induced SSEs on velocity-strengthening faults with characteristics comparable to those observed in several subduction zones (Perez-Silva et al., 2023). However, their model did not account for velocity-weakening behavior, which is also present in many slow slip regions (e.g., Ikari et al., 2020; Rabinowitz et al., 2018). Velocity-weakening friction has also been proposed as a key factor in SSE generation in several numerical models (e.g., Liu & Rice, 2005, 2007; Rubin, 2008; Segall et al., 2010). These mechanisms, however, have not been able to account for the ubiquitous nature of SSEs, as the range of parameters that produce them is relatively narrow.

In this study, we investigate whether periodic pore-pressure fluctuations can generate quasi-periodic SSEs on velocity-weakening faults, and whether this mechanism can broaden the conditions under which these SSEs occur. We build on the model by Perez-Silva et al. (2023) and extend it to account for velocity-weakening friction. To model pore-pressure fluctuations, we consider that fluids periodically permeate the fault at a localized region and subsequently diffuse along the fault plane. We then explore the characteristics of the pore-pressure perturbation (size, periodicity and amplitude) that generate SSEs comparable to observations, and derive implications for the hydraulic properties of the fault zone.

2. Methodology

To model long-term fault slip behavior, we use the simulation code developed by Lapusta and Liu (2009) and adapted to dip-slip by Kaneko et al. (2010). We consider a planar fault embedded in an infinite elastic medium and loaded by dip-slip velocity at the plate convergence rate. The fault's frictional interface is governed by rate-and-state friction, which describes the evolution of the friction coefficient f as a function of the slip rate V and a state variable θ (Dieterich, 1979; Linker & Dieterich, 1992; Marone, 1998):

$$f = f_0 + a \ln\left(\frac{V}{V_0}\right) + b \ln\left(\frac{V_0\theta}{D_{RS}}\right), \tag{1}$$

where f_0 is the steady-state friction coefficient at the reference rate V_0, D_{RS} is the characteristic slip distance for state evolution, and a and b are the direct and evolution effects, respectively. The evolution of the state variable is given by the aging law, modified to account for variations in normal stress (Linker & Dieterich, 1992):

$$\frac{d\theta}{dt} = 1 - \frac{V\theta}{D_{RS}} - \frac{\alpha\theta}{b\bar{\sigma}}\frac{d\bar{\sigma}}{dt}, \tag{2}$$

The parameter α describes the change in θ due to a step change in effective normal stress $\bar{\sigma}$, which is the difference between the lithostatic load and the pore fluid pressure. Based on laboratory measurements, α ranges from 0.2 to 0.3 (Hong & Marone, 2005; Linker & Dieterich, 1992; Richardson & Marone, 1999; Shreedharan et al., 2019). In this study, we set $\alpha = 0.2$.

The long-term slip behavior is governed by the following elastodynamic equation:

$$\tau(x,z;t) = f\left[\sigma - \Delta p_f(x,z;t)\right] = \tau_0 + F(x,z;t) - \frac{\mu}{2c_s}V(x,z;t), \tag{3}$$

Table 1
Model Parameters Used in This Study

Parameter	Symbol	Value
Characteristic slip distance	D_{RS}	5 mm
Direct effect in velocity-weakening patch	a	0.015–0.009
Evolution effect in velocity-weakening patch	b	0.016–0.011
Parameter from Linker and Dieterich (1992)	α	0.2
Background effective normal stress	σ	3 MPa (9 MPa)
Shear modulus	μ	10 GPa (30 GPa)
Critical nucleation size	$h^*_{RR} = \frac{\pi}{4}\frac{\mu D_{RS}}{\sigma(b-a)(1-\nu)}$	$\sim 8-17.5$ km
Reference friction coefficient	f_0	0.6
Reference slip velocity	V_0	10^{-6} m/s
Poisson's ratio	ν	0.25
Loading rate	V_{pl}	50 mm/yr
Spatial resolution	Δx	0.35–0.82 km

where τ is the shear stress, f is the friction coefficient (Equation 1), σ is the background effective normal stress (note that $\bar{\sigma} = \sigma - \Delta p_f(x,z:t)$) and $\Delta p_f(x,z;t)$ represents the change in pore-fluid pressure in space and time. On the right hand side, $\tau_0(x,z;t)$ is the initial shear stress, μ is the shear modulus, c_s is the shear wave speed, $V(x,z;t)$ is the slip rate and $F(x,z;t)$ accounts for wave-mediated stress transfers (Lapusta & Liu, 2009).

The fault consists of a velocity-weakening circular patch of radius R (with RSF parameters $a - b < 0$) surrounded by velocity-strengthening friction ($a - b > 0$). On velocity-weakening faults, the size of the patch that initiates unstable slip can be approximated by the theoretical estimate by Rice and Ruina (1983), based on linear stability analysis of stable sliding, in which $h^*_{RR} = \pi\mu^* D_{RS}/4(b - a)\sigma$. Alternatively, Rubin and Ampuero (2005) derived the upper bound of the nucleation size from the energy balance of a quasi-statically expanding crack. In this work, the nucleation size is given by h^*_{RR}, which we resolve by 15–30 cells to ensure good numerical resolution (Lapusta & Liu, 2009). The model parameters used in this study are given in Table 1 (see also Text S1 in Supporting Information S1).

To model pore-pressure changes $\Delta p_f(x,z;t)$ on the fault, we follow the Type II perturbation described in Perez-Silva et al. (2023). In this case, fluids are injected at the center of the fault and diffuse radially along the fault plane. Fluid flow occurs only within the fault plane and is fault-parallel and axisymmetric with respect to the axis of the circular cylinder (Sáez et al., 2022). Fluids diffuse from the cylinder wall along the fault plane over time t_{inj} and with diffusivity D. After t_{inj}, pore-pressure decreases as fluids diffuse away from the fault plane with diffusivity D_b (Figure 1d). The size of the perturbation is controlled by the diffusion length $\sqrt{Dt_{inj}}$ and its amplitude is given by the maximum pore-pressure change Δp_{max}. We consider D, t_{inj} and Δp_{max}, as input parameters. Pore-pressure perturbations are imposed periodically with a constant period T_{per}. An extended description of the modeling of pore-pressure changes is given in Text S2 in Supporting Information S1.

3. Model Results

3.1. Reference Models Without Pore-Pressure Perturbations

We first explore the parameter space of the reference model without pore-pressure perturbations, that is, assuming constant effective normal stress $\left(\sigma - \Delta p_f = \sigma\right)$. In this exploration, we assume mildly velocity-weakening behavior, where a/b varies linearly from ~0.81 to 0.94 and R ranges from 15 to 60 km, which corresponds to fault stiffness ratios ($2R/h^*_{RR}$) from 1.7 to 14.7. The choice of R is motivated by the expected size of the SSE slip region, which is on the order of tens of kilometers. As expected, we find three types of slip behavior: continuous creep, SSEs ($V_{max} < 10^{-2}$ m/s), and earthquakes ($V_{max} > 10^{-2}$ m/s), as shown in Figure 1c. Consistent with previous models (e.g., Liu & Rice, 2007), the SSE parameter space is transitional between that of continuous creep and regular earthquakes.

In the following, we examine how pore-pressure perturbations and their characteristics (size $\sqrt{Dt_{\text{inj}}}$, period T_{per}, and amplitude Δp_{max}), influence the slip behavior of the fault. Perturbations were applied only to simulations that originally exhibited continuous creep or SSEs (white circles and red squares in Figure 1c, respectively). This choice was guided by preliminary tests (not shown here), in which we imposed pore-pressure perturbations to reference simulations that generated earthquakes (blue stars in Figure 1c). These tests revealed that perturbations within the earthquake regime were not conducive to quasi-periodic SSEs, although they could induce sequences of earthquakes and SSEs.

3.2. Exploration of Pore-Pressure Perturbations

3.2.1. Perturbation Size

To examine the effect of the perturbation size $\sqrt{Dt_{\text{inj}}}$ on the fault slip behavior, we explored a range of D and t_{inj}. Specifically, we set D to 1, 10, 50 and 100 m^2/s and t_{inj} to 30 days, 6 months and 1 year. The explored perturbation characteristics were motivated by Perez-Silva et al. (2023) that found that comparable ranges lead to SSE properties consistent with observations in velocity-strengthening faults. To isolate the effect of the perturbation size, we set a constant amplitude $\Delta p_{\text{max}}/\sigma = 0.1$. In contrast, T_{per} was allowed to vary during the exploration because its effect could not be disentangled from that of the perturbation size $\sqrt{Dt_{\text{inj}}}$, as varying T_{per} for a given $\sqrt{Dt_{\text{inj}}}$ could lead to a range of slip behaviors (Section 3.2.2). To present the results of the exploration consistently, we adopted the following approach. Figure 2 shows cases in which a given value of T_{per} produced quasi-periodic SSEs, when such solutions were obtained. If no value of T_{per} led to quasi-periodic SSEs for a given $\sqrt{Dt_{\text{inj}}}$, we instead show results for slip behavior that still included SSEs, albeit non-periodic ones or mixed with earthquakes. For example, if a simulation with a given $\sqrt{Dt_{\text{inj}}}$ generated non-periodic SSEs for one value of T_{per} and, SSEs together with earthquakes for another, we presented the former in Figure 2. Finally, if the exploration of T_{per} only resulted in earthquakes, we presented that case. In Section 3.2.2, we discuss the effect of T_{per} and $\Delta p_{\text{max}}/\sigma$ on the fault behavior.

Applying pore-pressure perturbations of varying sizes changes the slip behavior of the fault, as shown in Figures 2a–2g, where Figure 2h shows the reference models without perturbations (same as Figure 1c). We distinguish three types of slip behavior in response to the perturbations: (a) *Repeating SSEs* (squares in Figure 2): SSEs induced by pore-pressure perturbations that occur with the same recurrence period and exhibit the same slip rate evolution. This slip behavior is comparable to quasi-periodic SSEs. (b) *Non-repeating SSEs* (diamonds in Figure 2): SSEs that do not follow a regular pattern, with variable recurrence intervals and different slip rate evolution. (c) *SSEs and earthquakes* (triangles in Figure 2), in which the same simulation gives rise to earthquakes and SSEs. (d) *Earthquakes* (stars in Figure 2): Earthquakes ($V_{\text{max}} > 10^{-2}$ m/s) induced by the pore-pressure perturbations. These results indicate that periodic pore-pressure perturbations broaden the range of fault slip behavior. For example, a fault that would otherwise undergo continuous creep can instead produce SSEs or earthquakes, depending on the characteristics of the imposed perturbation (cf., Figures 2a–2g and Figure 2h).

In general, repeating SSEs (squares in Figure 2) tend to emerge in models where small perturbations are imposed on more mildly velocity-weakening faults ($a/b \sim 1$) with a small fault stiffness ratio $2R/h^*{}_{\text{RR}}$. In other words, initially creeping faults subject to small pore-pressure perturbations tend to generate repeating SSEs. More complex fault responses (non-repeating SSEs or sequences of SSEs and earthquakes, diamonds and triangles in Figure 2, respectively) tend to be favored by conditions at the opposite range of the spectrum, namely larger perturbation sizes on faults with more strongly velocity-weakening faults and a larger fault stiffness ratio $2R/h^*{}_{\text{RR}}$.

3.2.2. Perturbation Period and Amplitude

In exploring the perturbation size (Section 3.2.1), we fixed $\Delta p_{\text{max}}/\sigma = 0.1$ and used a given value of T_{per} per simulation (colorbar in Figure 2). Here, we systematically explore $\Delta p_{\text{max}}/\sigma$ and T_{per} to investigate their influence on the fault response. For that purpose, we apply pore-pressure perturbations to an example simulation with $R = 30$ km and $a/b = 0.94$ (black arrow in Figure 2h) and consider two exploration cases. First, we explore T_{per}

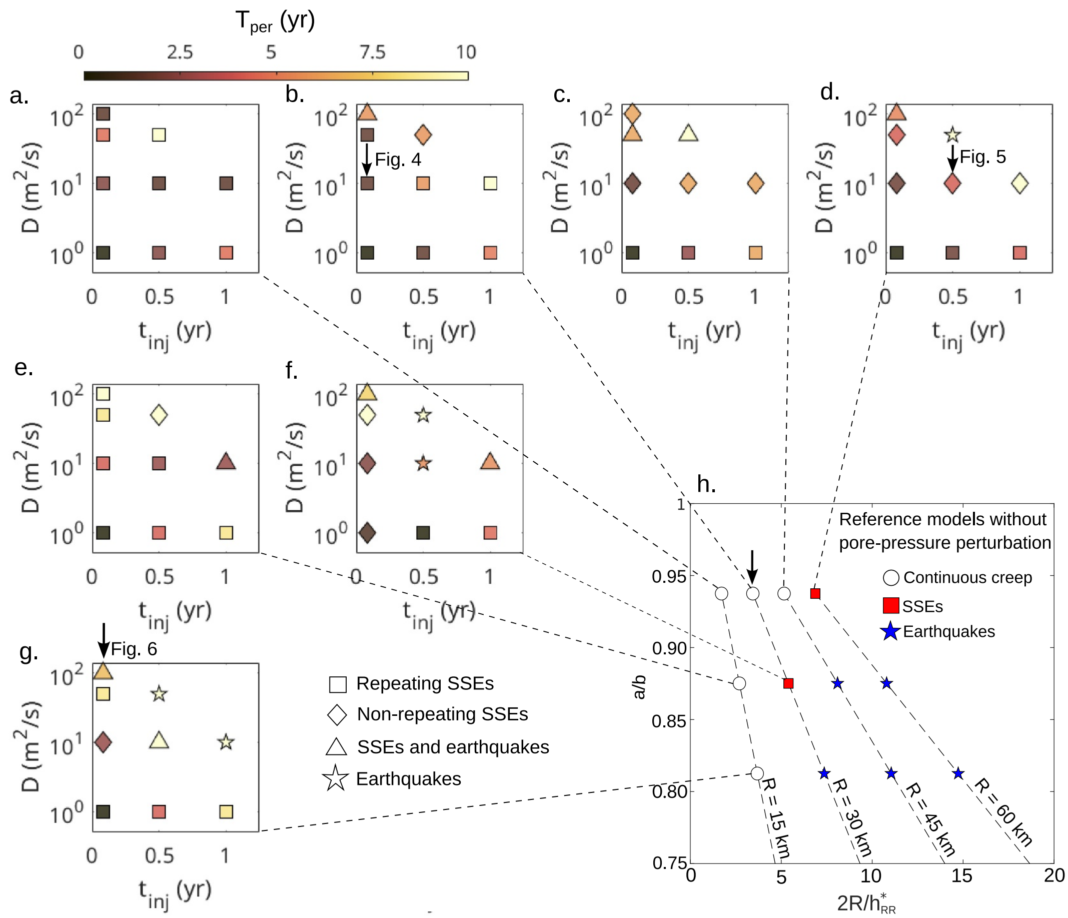

Figure 2. (a–g) Phase diagram showing the fault response to pore-pressure perturbations with characteristics described by parameters D, t_{inj} and T_{per}, with the latter shown in the colorbar. The fault response is classified into repeating SSEs (squares), non-repeating SSEs (diamonds), SSEs and earthquakes (triangles) and only earthquakes (stars). A description of each slip behavior is given in Section 4. Perturbations are applied to reference simulations cases (without pore-pressure perturbations) shown in (h), excluding cases that led to earthquakes.

from 1 to 20 yr assuming different perturbation sizes, $1\ \text{m}^2/\text{s} < D < 100\ \text{m}^2/\text{s}$ with $t_{\text{inj}} = 30$ days, and a constant $\Delta p_{\max}/\sigma = 0.1$. Second, we explore $\Delta p_{\max}/\sigma$ from 0.1 to 0.7 at different values of T_{per}, while setting a constant perturbation size ($D = 10\ \text{m}^2/\text{s}$ and $t_{\text{inj}} = 30$ days, $\sqrt{Dt_{\text{inj}}}/h^*_{\text{RR}} = 0.3$). The results of the exploration are shown in Figure 3, where we classify the fault response to the applied perturbations. The same slip behaviors defined in Figure 2 emerge, with one additional case, namely, (e) *Induced SSEs followed by quasi-spontaneous SSEs*. For this case, pore-pressure perturbations induce SSEs, which are followed by quasi-spontaneous SSEs that do not occur simultaneously with the pore-pressure perturbation.

Repeating SSEs in Figure 3a only arise for certain combinations of $\sqrt{Dt_{\text{inj}}}$ and T_{per}. Thus, to find the parameter space favorable for these SSEs, we cannot consider the perturbation period separately from the perturbation size, as mentioned in Section 3.2.1. This is because the fault response to the perturbation period T_{per} also depends on the slip history, which is itself affected by the characteristics of the perturbation (i.e., its size and amplitude). In Section 4, we present cases that exemplify this interplay. The combined effect of these parameters explains why systematic patterns are difficult to identify when exploring one or two parameters independently, as reflected in Figures 2 and 3.

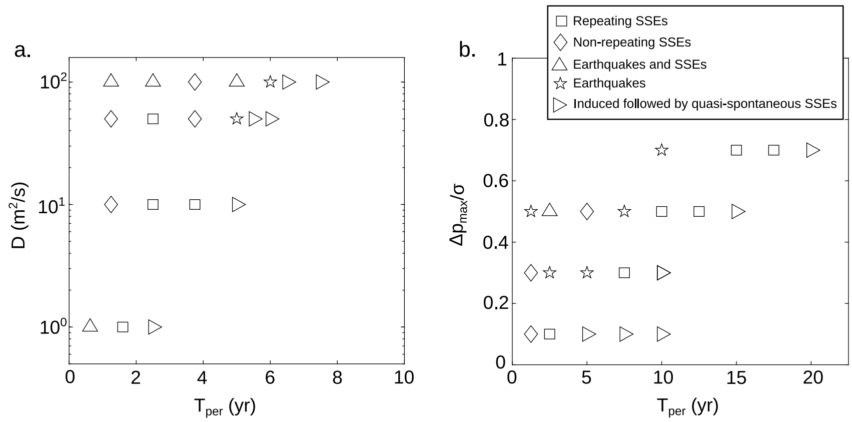

Figure 3. Phase diagrams illustrating the fault response with respect to (a) T_{per} and D (assuming constant $t_{\mathrm{inj}} = 30$ days), and (b) T_{per} and $\Delta p_{\mathrm{max}}/\sigma$. In (a) and (b), we assume the reference model with $R = 30$ km and $a/b = 0.94$. For (a), we set $\Delta p_{\mathrm{max}}/\sigma = 0.1$. For (b), we assume a constant perturbation size with $\sqrt{Dt_{\mathrm{inj}}}/h^*_{\mathrm{RR}} = 0.3$ ($D = 10$ m^2/s, $t_{\mathrm{inj}} = 30$ days and $h^*_{\mathrm{RR}} = 17.5$ km). The reference model for (a) and (b) corresponds to the case with $R = 30$ km and $a/b = 0.94$.

4. Fault Response to Pore Pressure Perturbations

In this section, we describe the fault response to pore-pressure perturbations. We focus on slip behaviors (a) Repeating SSEs, (b) Non-repeating SSEs and (c) SSEs and earthquakes, while (d) Earthquakes and (e) Induced and quasi-spontaneous SSEs (Section 3.2.2) are explained in Text S3 in Supporting Information S1. In addition, we describe the effect of parameter α in Text S5 in the Supporting Information S1.

4.1. Repeating SSEs

To illustrate the fault behavior during induced repeating SSEs, we consider an example case with $R = 30$ km and $a/b = 0.94$, subjected to a periodic pore-pressure perturbation characterized by $D = 10$ m^2/s, $t_{\mathrm{inj}} = 30$ days, $\Delta p_{\mathrm{max}}/\sigma = 0.1$ and $T_{\mathrm{per}} = 2.5$ yr (black arrow in Figure 2b). Figure 4a shows the temporal evolution of $V_{\mathrm{max}}/V_{\mathrm{pl}}$, while Figure 4b displays the evolution of slip velocity V (m/s), shear stress τ, and effective normal stress $\sigma - \Delta p_{\mathrm{f}}$ at $x = 0$, $z = 2$ km. We also include the evolution of $\Omega = V\theta/D_{\mathrm{RS}}$, which represents the proximity to steady state. $\Omega = 1$ corresponds to steady state sliding, $\Omega > 1$ and $\Omega < 1$ to sliding above and below steady state, respectively (Perfettini & Ampuero, 2008).

The first perturbation at $t = 25$ yr causes a transient increase in $V_{\mathrm{max}}/V_{\mathrm{pl}}$ (solid black line in Figure 4a), and a decrease in the shear stress τ (dashed blue line in Figure 4b). A similar pattern repeats itself in the following perturbations. After the first few perturbations ($t = 40$ yr), the fault develops a regular pattern in which the slip velocity increases close to three orders of magnitude above the plate rate during pore-pressure increase, accompanied by a decrease in shear stress τ. This behavior can be explained by Equation 3, in that the decrease in effective normal stress is balanced by a decrease in shear stress and an increase in the frictional strength f through V. The opposite occurs during depressurization, when f decreases due to a decrease in slip velocity V to compensate for the decrease in $\sigma - \Delta p_{\mathrm{f}}$. The shear stress does not immediately return to its pre-perturbation level. Instead, it gradually increases in the period between perturbations, while the previously perturbed fault region remains locked ($V < V_{\mathrm{pl}}$). The fault response is illustrated in the evolution of Ω (red line in Figure 4b). Perturbations are applied when the fault is slightly above steady state ($\Omega > 1$), but once the perturbation finishes, the fault is below steady-state ($\Omega < 1$). The fault gradually approaches steady state in the period between perturbations, with Ω increasing from below 1 toward 1. The increase in τ during the period between perturbations correlates with the return of the fault to steady state.

The spatiotemporal evolution of field variables $\Delta p_{\mathrm{f}}/\sigma$, $\log_{10}(V/V_{\mathrm{pl}})$, τ and $\log_{10}\Omega$ over the time interval 50 yr $< t <$ 50.5 yr is shown in Figures 4c–4f (see also Movie S1). The fault response can be divided into three consecutive phases, as explained in the following. (a) As pore-pressure increases (Figure 4c), the slip front migrates from the edges of the perturbed area to the center of the fault (converging arrows in Figure 4d), where they reach peak velocity, while τ also increases following the slip front migration (Figure 4e). During this phase,

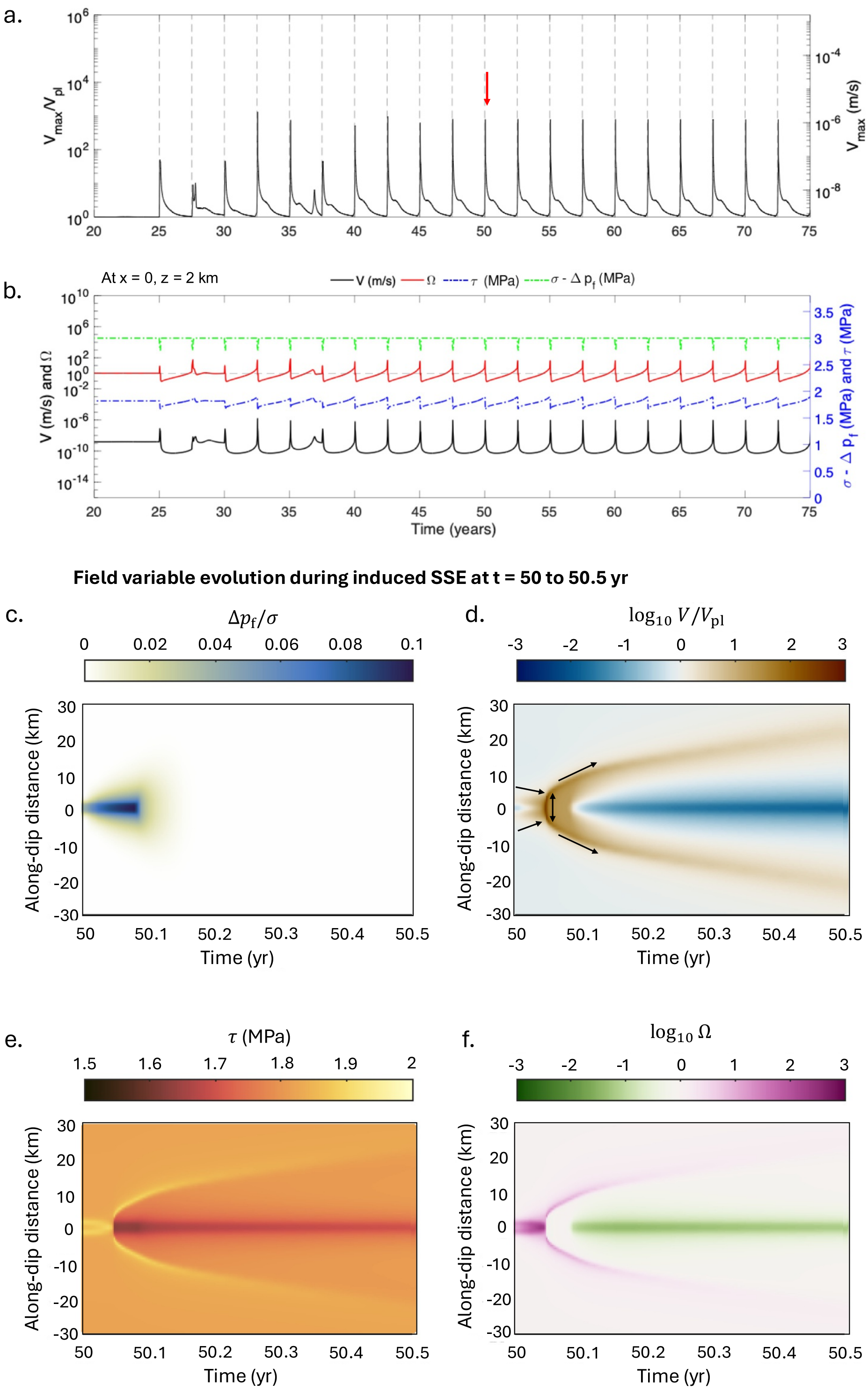

Figure 4. Example of repeating SSEs in a simulation with $R = 30$ km and $a/b = 0.94$; and pore-pressure perturbation parameters $D = 10\ m^2/s$, $t_{inj} = 30$ days, $\Delta p_f/\sigma = 0.1$, and $T_{per} = 2.5$ years. (a) Evolution of maximum slip rate on the fault (V_{max}) over time. Vertical dashed lines mark the start time of each perturbation, with the first perturbation applied at $t = 25$ years. (b) Temporal evolution of field variables slip rate (V, solid black line), distance to steady state (Ω, solid red line), shear stress (τ, dashed blue line), and effective normal stress ($\sigma - \Delta p_f$, dashed green line) at $x = 0$ and $z = 2$ km. The dashed black line indicates $\Omega = 1$. (c–f) Spatiotemporal evolution along depth during one induced SSE of (c) $\Delta p_f/\sigma$, (d) $\log_{10}(V/V_{pl})$ (e) τ and (f) $\log_{10}\Omega$. $\Omega = V\theta/D_{RS}$ measures the proximity to steady state, where $\Omega = 1$ is at steady state, $\Omega > 1$ is above steady state and $\Omega < 1$ is below steady state. Black arrows in (d) indicate phases of slip rate evolution (see text for details).

10.1029/2025GC012823

the fault remains above steady state, as seen by the positive value of $\log_{10}\Omega$ (Figure 4f). (b) Once peak velocity is reached, a crack develops (vertical arrow in Figure 4d) and crack expansion follows as slip velocity fronts migrate away from the injection point (diverging arrows in Figure 4d). During crack expansion, the slip rate is higher at the tip of the crack, and $\log_{10}\Omega \sim 0$ inside the crack, indicating that the fault is close to steady state in that region (Figure 4f). (c) During pore-pressure decrease at $t = 50.08$ yr, field variables $\Delta p_{\max}/\sigma$, $\log_{10}(V/V_{\mathrm{pl}})$, τ and $\log_{10}\Omega$ decrease, starting from the center of the fault. After the perturbation, the pressurized area remains locked and below steady state ($\log_{10}\Omega < 0$, Figure 4f).

4.2. Non-Repeating SSEs

Non-repeating SSEs represent a complex slip behavior in which the fault response exhibits an irregular, yet aseismic, slip pattern. To illustrate this case, we consider a simulation with $R = 60$ km and $a/b = 0.94$, which originally produced spontaneous SSEs (red square with $R = 60$ km in Figure 2h). We applied periodic pore-pressure perturbations to this fault, characterized by $D = 10$ m^2/s, $t_{\mathrm{inj}} = 0.5$ yr, $\Delta p_{\max}/\sigma = 0.1$ and $T_{\mathrm{per}} = 5$ yr (black arrow in Figure 2d). The fault response to the perturbations is characterized by SSEs with variable slip rate evolution and peak velocities between 1 and 6 orders of magnitude above the plate rate (Figure 5a). We classify the emerging SSEs into two types: instantaneously induced SSEs and delayed onset SSEs, depending on the timing of the fault response following each perturbation, as will be discussed next.

To explain the fault behavior in each case, we show the temporal evolution of V, Ω, τ and $\sigma - \Delta p_{\mathrm{f}}$ at $x = 0$ and $z = 2$ km in Figure 5b. During instantaneously induced SSEs, the slip rate increases simultaneously with the pore-pressure increase, while the shear stress τ decreases (e.g., I-SSE at $t = 35$ yr Figure 5a, see also V and τ in Figure 5b), thus following a behavior comparable to that of repeating SSEs (Section 4.1). In contrast, some perturbations initially induce a small and transient increase in V that remains below the plate rate (e.g., $V < V_{\mathrm{pl}}$ at $t = 40$ yr in Figure 5b), followed by a larger acceleration, during which the slip rate increases by between 4 and 6 orders of magnitude above the plate rate (e.g., DO-SSE in Figure 5a). We term this case a delayed-onset SSE.

Whether a perturbation induces SSEs instantaneously or produces a delayed response depends on the timing of the perturbations with respect to the slip history and the evolution of shear stress. In this example, when the perturbation is imposed at steady state ($\Omega = 1$, red line in Figure 5b), it generates an immediate increase in slip velocity V. In contrast, when the perturbation is imposed below steady state ($\Omega < 1$), even though V increases, slip is not significant ($V < V_{\mathrm{pl}}$). The difference in the fault response can be explained through Equation 3. For instantaneously induced SSEs, the fault response resembles that of repeating SSEs (Section 4.1), that is, an increase in Δp_{f} is compensated by an increase in f through V and a decrease in τ. For delayed-onset SSEs, even though V and f increase during the perturbation, τ remains approximately constant (dashed blue line in Figure 5b). Only later does τ drop, allowing significant slip to occur. This behavior arises because, once an induced SSE occurs, τ drops beneath its initial value and then gradually recovers as slip accumulates. If a perturbation takes place before τ has sufficiently recovered, it cannot induce an instantaneous SSE.

We plot the spatio-temporal evolution of $\Delta p_{\mathrm{f}}/\sigma$, $\log_{10}(V/V_{\mathrm{pl}})$ and τ to examine the fault response during instantaneously-induced SSEs (Figures 5c–5e, see also Movie S2) and delayed-onset SSEs (Figures 5f–5h, see also Movie S3). For instantaneously-induced SSEs, pressurization leads to an increase in the slip rate at the center of the fault, followed by a crack growth and expansion phase (divergent arrows in Figure 5d), during which slip fronts migrate radially along the fault and propagate beyond the pressurized zone (cf., Figures 5c and 5d). During this phase, τ is highest at the slip front (Figure 5e). Notably, crack expansion continues even after pore-pressure begins to decline. At this stage, the slip rate —starting from the center of the fault—begins to decrease (Figure 5d), accompanied by a reduction in shear stress τ (Figure 5e). For delayed-onset SSEs, slip rate acceleration occurs after the perturbation has finished (cf., Figures 5f and 5g). In this case, two slip fronts migrate toward the center of the fault (converging arrows in Figure 5g) and induce slip acceleration at the fault center. Following this acceleration, the slip fronts migrate radially away from the fault center (divergent arrows in Figure 5g, respectively). Note that after the delayed-onset SSEs, the fault slip velocity remains close to V_{pl} in the perturbed region, in contrast to instantaneously induced SSEs, in which it remains below V_{pl} (cf., Figures 5d and 5g after the SSE has occurred).

10.1029/2025GC012823

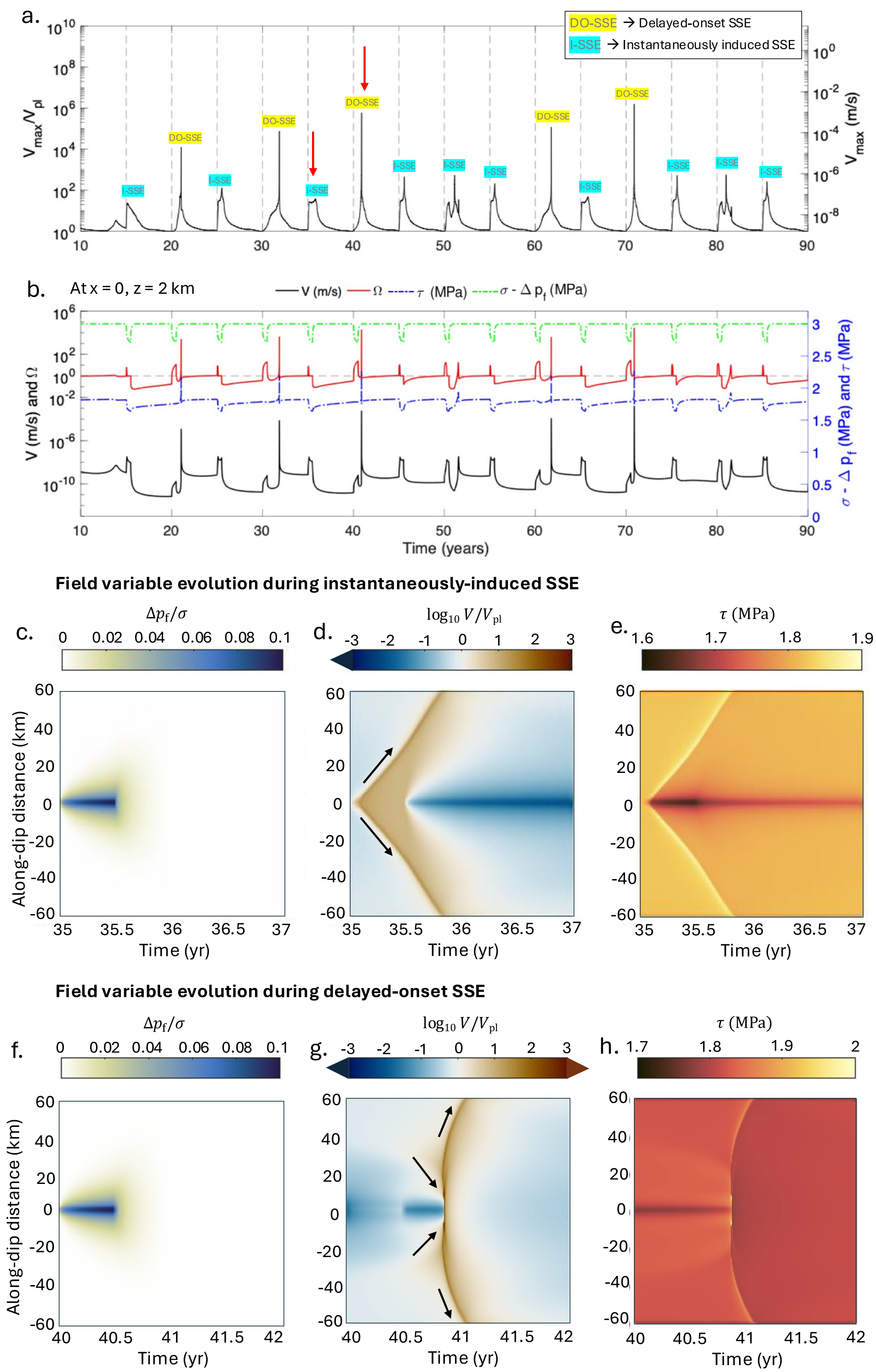

Figure 5. Example of non-repeating SSEs in a simulation with $R = 60$ km and $a/b = 0.94$; and pore-pressure perturbation parameters $D = 10$ m^2/s, $t_{\text{inj}} = 0.5$ year, $\Delta p_f/\sigma = 0.1$, and $T_{\text{per}} = 5$ years. (a) Evolution of maximum slip rate ($V_{\max}$) over time. Vertical dashed lines mark the start time of each perturbation, with the first perturbation at $t = 15$ years. First and second red arrows indicate the events shown in (c–e) and (f–h), respectively. (b) Temporal evolution of slip velocity (V, solid black line), distance to steady state (Ω, solid red line), shear strength (τ, dashed blue line), and effective normal stress ($\sigma - \Delta p_f$, dashed green line) at $x = 0$ and $z = 2$ km. The dashed black line indicates $\Omega = 1$. (c–h) Spatiotemporal evolution along depth of (c–f) p_f/σ, (d–g) V/V_{pl} and (e–h) τ over two different time periods illustrating (c–e) an instantaneously-induced SSE and (f–h) a delayed-onset SSE. Black arrows in (d and g) indicate the direction of slip-front migration.

4.3. SSEs and Earthquakes

In some simulations, pore-pressure perturbations induce both SSEs and earthquakes. An example is illustrated in Figure 6, where we apply a pore-pressure perturbation characterized by $D = 100$ m^2/s, $t_{\mathrm{inj}} = 30$ days, $\Delta p_{\max}/\sigma = 0.1$ and $T_{\mathrm{per}} = 4$ yr (black arrow in Figure 2g) to a continuously creeping fault ($R = 15$ km and $a/b = 0.81$, Figure 2h). The evolution of maximum slip rate on the fault in Figure 6a illustrates an irregular slip pattern, in which the slip rate increases between two and eight orders of magnitude above the background plate-loading rate after each perturbation. Some of the induced events are instantaneously induced SSEs (I-SSE in Figure 6a) and delayed onset SSEs (DO-SSE in Figure 6a), as described in Section 4.2, while others are earthquakes ($V_{\max} > 10^{-2}$ m/s, I-Eqk in Figure 6a) and aborted slip events (A-Slip in Figure 6a). The latter are characterized by slip rate accelerations at the edges of the velocity-weakening patch but not within the patch, where the fault remains locked.

Delayed-onset SSEs and instantaneously induced SSEs emerge under similar conditions to those described in Section 4.2. Aborted slip events represent the initial phase of delayed-onset SSEs and occur when the perturbation takes place while the fault is below steady state ($\Omega < 1$) and τ has not yet recovered enough to drop again across the fault. Earthquakes also occur when $\Omega < 1$ at the time of perturbation, but in this case the shear stress has recovered sufficiently. Earthquake occurrence can be attributed to the large perturbation size (Figure 2), which significantly weakens the fault. The drop in $\sigma - p_{\mathrm{f}}$ initially causes an increase in f through V, but as slip rate continues to rise, inertial effects and elastic stress transfers (right hand side of Equation 3) become significant, leading to a large drop in τ. Although both aborted slip events and earthquakes occur when the fault is below steady-state ($\Omega < 1$), the resulting slip behavior following a perturbation is difficult to predict. This is because it depends on the evolution of τ, which is in turn affected by the slip history.

In Figure 6, we show examples of the spatial and temporal evolution of $\Delta p_{\mathrm{f}}/\sigma$, $\log_{10}(V/V_{\mathrm{pl}})$ and τ for induced earthquakes (Figures 6c–6e, see also Movie S4) and induced SSEs (Figures 6f–6h, see also Movie S5), while Figure S3 in Supporting Information S1 shows the field variable evolution during aborted slip events and delayed-onset SSEs. The slip rate evolution between induced earthquakes and induced SSEs follows a similar pattern, characterized by four phases: (a) Slip rate acceleration, (b) crack growth, (c) crack expansion, and (d) slip deceleration, which starts at the onset of depressurization. In terms of slip rate evolution, the main difference is that for SSEs, the slip acceleration starts at the injection point, and the crack growth phase takes a longer time (divergence arrows for $t < 80.1$ yr in Figure 6g), whereas for earthquakes, the slip acceleration starts as two slip fronts converge (convergent arrows in Figure 6d), and the crack growth phase is faster (vertical arrow at $t = 82.1$ yr, see also Movies S4 and S5).

5. Properties of Induced Repeating SSEs

To examine the range of SSE properties induced by the pore-pressure perturbations, we estimate the properties of repeating SSEs found in our parameter exploration (squares in Figures 2a–2g and Figure 3). We focus on first-order properties, namely, duration, magnitude and stress drop, which we calculate as explained below. First, we set a velocity threshold $V_{\mathrm{thr}} = 0.3$ mm/day, which is within the resolution range of GNSS stations that detect SSEs (e.g., ~0.25–0.5 mm/day, Wech & Bartlow, 2014). Then, we define SSE duration as the time over which the maximum slip rate on the fault exceeds V_{thr}. We calculate the corresponding SSE moment using the SSE area and the slip accumulated over the SSE duration. To calculate the accrued slip, we consider the slip over the cells with slip larger than a minimum slip, defined as $1.1 \times V_{\mathrm{pl}} \times$ SSE duration. This definition ensures that the accumulated slip exceeds the slip accrued due to the plate loading rate over the SSE duration. Note that to calculate SSE magnitude, we assume a shear modulus $\mu = 30$ GPa, instead of 10 GPa (Table 1), as we will later compare these results with previous models that assume the same value. To keep h^*_{RR} constant after the change in μ, we also set σ to 9 MPa, instead of 3 MPa (Table 1). This ensures that both cases exhibit the same slip behavior. To calculate SSE stress drop, we used the energy-based approach by Noda et al. (2013). In this approach, the stress drop $\Delta\sigma_{\mathrm{E}}$ is calculated by averaging the stress change distribution with the final slip cell as the weighting function (Noda et al., 2013): $\overline{\Delta\sigma_E} = \oint_\Sigma \Delta\sigma\, \Delta u\, dS / \oint_\Sigma \Delta u\, dS$, where Σ is the SSE source area, which corresponds to the region with slip greater than the minimum slip defined above, Δu is the final slip distribution of the SSE, and $\Delta\sigma$ is the difference between the shear stress distribution at the start of the SSE and at the end of the SSE. Δu and $\Delta\sigma$ depend on SSE duration and thus on V_{thr}.

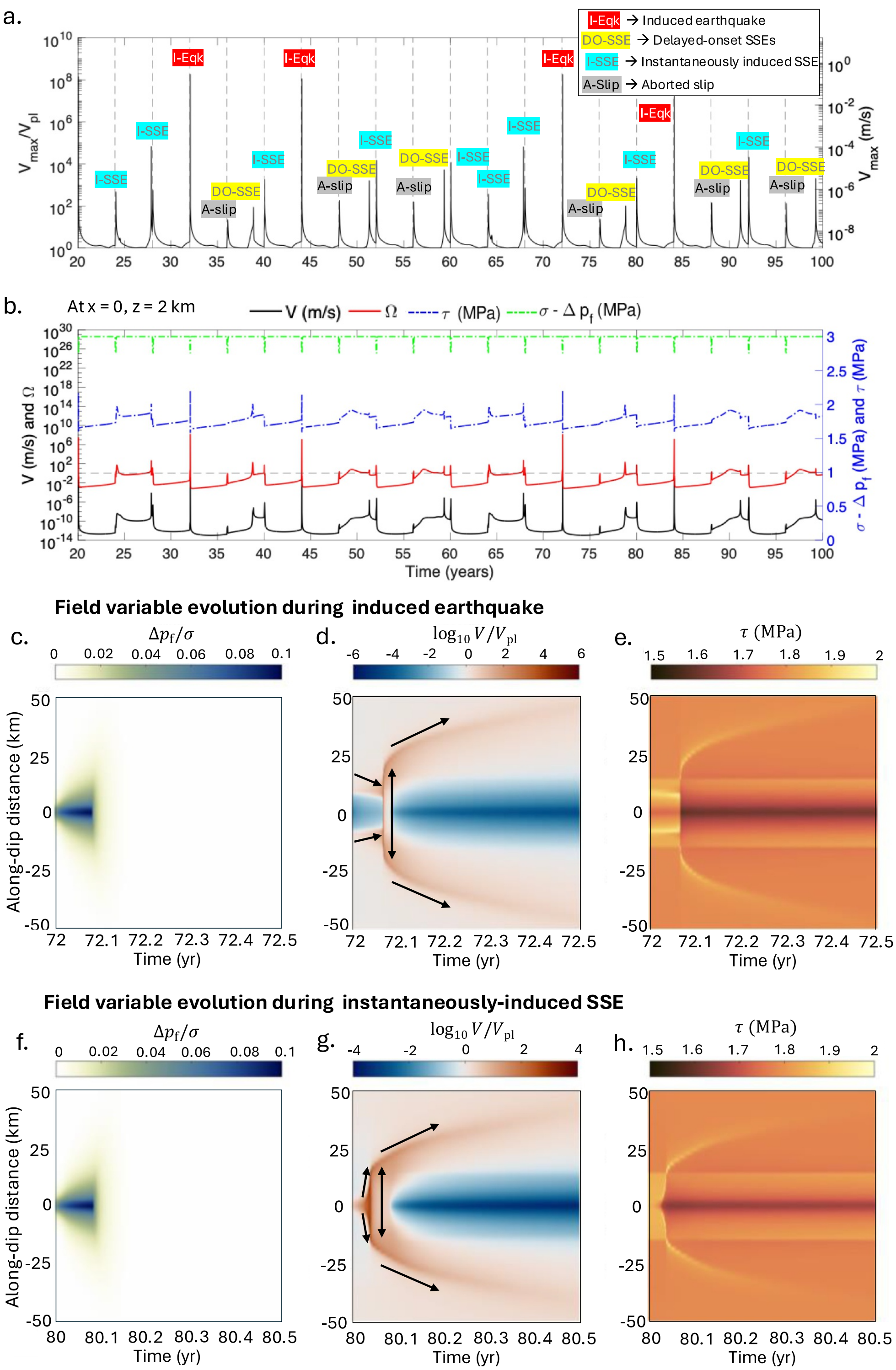

Figure 6. Example of induced SSEs and earthquakes in a simulation with $R = 15$ km and $a/b = 0.81$; and pore-pressure perturbation parameters $D = 100$ m^2/s, $t_{\mathrm{inj}} = 30$ days, $\Delta p_f/\sigma = 0.1$, and $T_{\mathrm{per}} = 4$ years. (a) Evolution of slip rate ($V_{\max}$) over time. Vertical dashed lines mark the start time of each perturbation, with the first perturbation initiated at $t = 25$ years. (b) Temporal evolution of field variables slip velocity (V, solid black line), distance to steady state (Ω, solid red line), shear strength (τ, dashed blue line), and effective normal stress ($\sigma - \Delta p_f$, dashed green line) at $x = 0$ and $z = 2$ km. The dashed black line indicates $\Omega = 1$. (c–h) Spatiotemporal evolution along depth during (c–e) one induced earthquake and (f–h) one instantaneously-induced SSE of field variables (c–f) p_f/σ, (d–g) $\log_{10}(V/V_{\mathrm{pl}})$, (e–h) τ. Black arrows in (d and g) indicate the direction of slip-front migration.

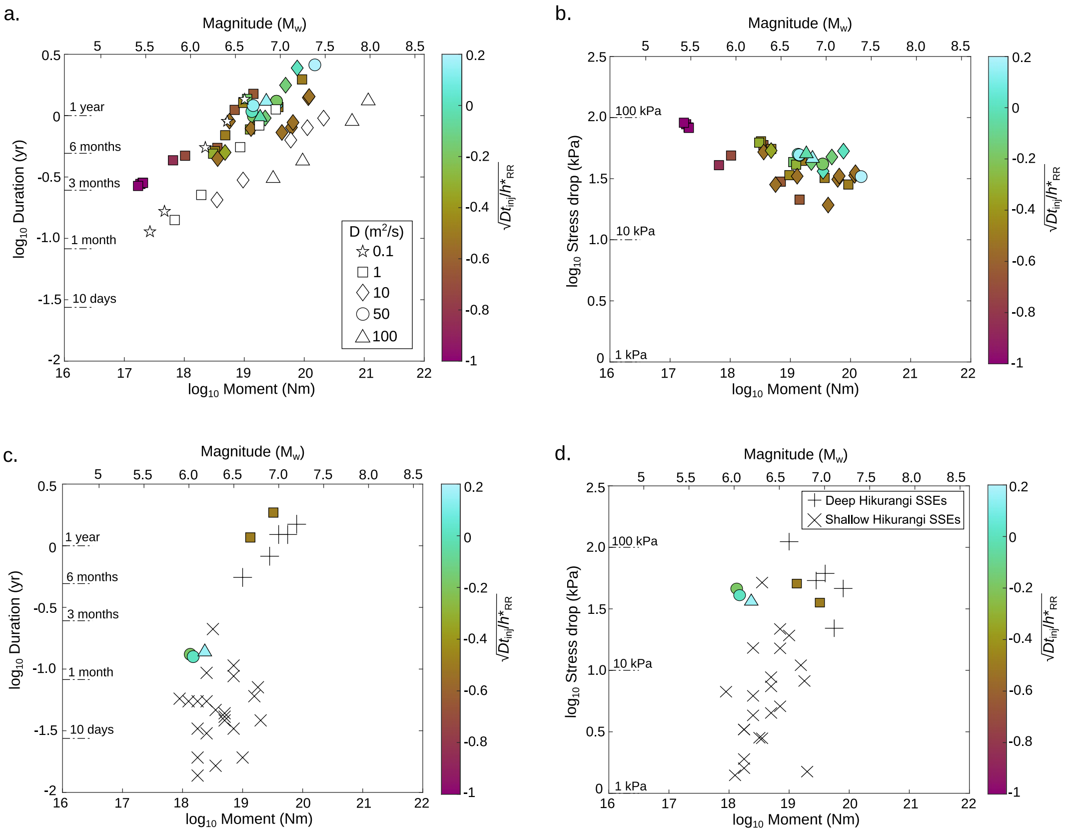

Figure 7. (a, b) Source properties of induced repeating SSEs from Figures 2 and 3. (a) Average duration and magnitude of repeating SSEs. White symbols denote results from simulations assuming velocity-strengthening friction properties (as shown in Figure 9a of Perez-Silva et al., 2023). (b) Average stress drop and magnitude of repeating SSEs. The colorbar represents the characteristic length scale $\log_{10}\left(\sqrt{Dt_{\text{inj}}}/h^*_{\text{RR}}\right)$. (c, d) Observed source properties of Hikurangi SSEs and comparison with model results. (c) Observed duration and magnitude of deep (+ symbol) and shallow (× symbol) Hikurangi SSEs (data compiled from Ikari et al., 2020; Wallace, 2020; and Warren-Smith et al., 2019). (d) Observed stress drop and magnitude of deep and shallow SSEs. Colored symbols in (c and d) indicate the source properties of induced repeating SSEs that best match the observed properties of Hikurangi SSEs. Note that each symbol represents a different hydraulic diffusivity value D as shown in legend, see (a).

We plot the average moment and duration of repeating SSEs in each simulation along with the corresponding normalized perturbation size $\sqrt{Dt_{\text{inj}}}/h^*_{\text{RR}}$ in Figure 7a. Figure S5 in Supporting Information S1 shows the results for the original values of μ and σ. Repeating SSE magnitudes range from ~M_w 5.5 − 7.5, while SSE durations span from ~3 months to over a year (Figure 7a). Consistent with Perez-Silva et al. (2023), larger perturbation sizes tend to induce repeating SSEs with longer durations and larger magnitudes (Figure 7a). Notably, the properties of repeating SSEs cover a narrow range that is skewed toward long-duration events, while short-duration and large-magnitude SSEs are not reproduced. For comparison, we also plot the properties of SSEs induced by pore-pressure perturbations in a velocity-strengthening fault (white symbols in Figure 7a, after figure 9a in Perez-Silva et al., 2023). In velocity-strengthening faults, induced SSEs display a wider range of source properties. The stress drops of induced repeating SSEs in velocity-weakening faults are within 10–100 kPa (Figure 7b), while the magnitude of the pore-pressure change ranges from 0.3 to 2.1 MPa.

To assess whether induced repeating SSEs could reproduce properties comparable to observed SSEs, we plot the observed duration and moment of SSEs along the deep and shallow Hikurangi margin (plus and cross symbols in Figure 7c, respectively), as estimated by geodetic inversions (e.g., Wallace, 2020; Wallace & Beavan, 2010). Then, using simulations shown in Figure 7a as a reference, we further explore the parameter space to identify models that generated repeating SSEs with durations and moments similar to shallow and deep Hikurangi SSEs. The selected models are shown in Figure 7c and model parameters are given in Table S1 in Supporting Information S1. We note that to calculate the properties of simulated shallow Hikurangi SSEs, we set a higher velocity

10.1029/2025GC012823

threshold (~2 mm/day), to account for the fact that these events occur offshore, where the sensitivity of inland GNSS stations is lower. Although repeating SSEs in our model roughly capture Hikurangi SSE properties, the model fails to reproduce shallow Hikurangi SSEs with short durations (<1 month) and large magnitudes (>M_w6.5). We attribute this to the relatively narrow range of SSE properties captured by the model (Figure 7a). We also compare the stress drop constrained by observations with that of our preferred models in Figure 7d. For deep SSEs, the model captures the order of magnitude of stress drop (10 s–100 kPa), while for shallow SSEs, the model is skewed toward larger stress drops (~30 kPa) than those expected from observations (~1–50 kPa).

6. Discussion

6.1. Effect of Pore-Pressure Perturbations on Velocity-Weakening Fault Regions

Our results show that periodic pore-pressure perturbations induce a range of slip behaviors on velocity-weakening faults (Figures 2a–2g). The type of induced slip behavior depends on both the properties of the perturbations (size $\sqrt{Dt_{\text{inj}}}$, amplitude $\Delta p_{\max}/\sigma$ and perturbation period T_{per}, Figures 2 and 3) and the properties of the frictional interface (a/b, fault stiffness ratio $2R/h^*_{\text{RR}}$, Figure 2). However, the effect of individual parameters on the fault response cannot be considered independently. For example, the fault response to the perturbation size varies with the perturbation period (Figure 3a). This occurs because the slip behavior induced by pore-pressure perturbations also depends on the conditions at the time of each perturbation (slip rate, state variable and shear stress), and the evolution of shear stress, all of which are affected by the slip history of the fault. At the same time, the slip history itself is shaped by the properties of the perturbation. Thus, the long-term slip behavior is the result of a complex interplay between the pore-pressure perturbations and the evolving slip history of the fault.

We identify and classify the fault response to pore-pressure perturbations into five different types of slip behaviors, ranging from repeating SSEs to earthquakes, including mixed behavior such as irregular SSEs and earthquakes (Section 4). We focus on describing the conditions that favor quasi-periodic SSE generation, which is the primary aim of this study. Our parameter exploration shows that repeating SSEs (i.e., SSEs with the same properties, slip rate evolution and periodic recurrence intervals), which are comparable to quasi-periodic SSEs, are induced in velocity-weakening fault regions by a range of pore-pressure perturbations and friction properties (Figure 2). Most repeating SSEs in our exploration arise after imposing small perturbations on originally creeping faults (Figures 2a–2c, 2e, and 2g). Repeating SSEs also arise in cases where the slip behavior of the reference model (without pore-pressure perturbations) corresponds to spontaneous SSEs. In this case, the characteristics of the induced SSEs are different from those of the spontaneous SSEs. These results indicate that applying pore-pressure perturbations to velocity-weakening fault regions expands the parameter space that leads to SSEs (cf., Figures 2a–2g and Figure 2h). However, SSE generation remains constrained by the W/h^*_{RR} criterion (Liu & Rice, 2007), as quasi-periodic SSEs in our model occur primarily in creeping faults, which requires low W/h^*_{RR}.

6.2. Induced SSE Properties

Pore-pressure perturbations can induce repeating SSEs with different durations and magnitudes, which range from ~3 months to over a year and M_w 5.5 − 7.5 (Figure 7a). Consistent with Perez-Silva et al. (2023), induced SSE duration and magnitude positively correlate with the change in the perturbation size $\left(\sqrt{Dt_{\text{inj}}}/h^*_{\text{RR}}\right)$. Thus, larger perturbation sizes lead to SSEs with larger magnitudes and longer durations (Figure 7a). The stress drops of induced SSEs are between 10 and 100 kPa (Figure 7b), which is within the range expected for SSEs (10–1,000 kPa; Gao et al., 2012). Notably, these stress drops are lower than the imposed pore-pressure change (300–2,100 kPa), which is consistent with observations in that inferred pore-pressure change during SSEs (~ 1 to 10 MPa; Gosselin et al., 2020) is larger than SSE stress drop.

The model also reproduced SSE durations and magnitudes comparable to those of shallow and deep Hikurangi SSEs (Figure 7c). However, it fails to capture the broad range of SSE properties observed at Hikurangi. Compared with velocity-strengthening faults subject to pore-pressure perturbations, SSE properties induced in velocity-weakening faults span a narrower range (cf., white and colored symbols in Figure 7a). In addition, models of velocity-strengthening faults can reproduce a broader range of observed SSE properties in different subduction zones, including those at Hikurangi (cf., Figure 7b and figure 9b in Perez-Silva et al., 2023). This suggests that

10.1029/2025GC012823

pore-pressure perturbations on velocity-strengthening faults are a more plausible explanation for observed SSEs than those on velocity-weakening faults.

6.3. Implications for the SSE Generation Environment

Our results indicate that for velocity-weakening faults subjected to periodic pore-pressure perturbations to reproduce SSE properties comparable to observations, very high hydraulic diffusivities are required (1 $m^2/s < D < 100\ m^2/s$). Such values are several orders of magnitude larger than inferred hydraulic diffusivity values in subduction zones (Saffer & Tobin, 2011; Xue et al., 2013), and correspond to permeabilities in the range of 5×10^{-12} to $5 \times 10^{-10}\ m^2$ (see Text S4 in Supporting Information S1). These values contrast with the estimated background permeability of intact rock, which ranges from 10^{-24} to $10^{-17}\ m^2$ (Ganzhorn et al., 2019; Katayama et al., 2012; Kawano et al., 2011; Muñoz-Montecinos & Behr, 2023; Skarbek & Saffer, 2009). This discrepancy could be reconciled with transient changes in fault zone properties during SSEs, as suggested by field observations that estimate permeability increases of 3 and 8 orders of magnitude at the source depths of both shallow and deep SSEs (Muñoz-Montecinos & Behr, 2023, and references therein). Our model also indicates that the timescales of hydraulic diffusion range from a few weeks to one year. Further constraints on fault zone permeability during SSEs are required to test the model predictions.

6.4. Comparison to Hydromechanical Models of Slow Slip

In our model, pore-pressure perturbations affect fault slip by reducing the fault strength and thus weakening the fault. However, the relation between fluid flow and fault slip is much more complex, as it depends on several hydrological variables (e.g., fluid production rate, permeability, specific storage, porosity). Recent models have explored this complexity by modeling a two-way coupling between fault slip and fluid flow. Ozawa et al. (2024) modeled the evolution of permeability, fluid flow and pore pressure in a 2D model. Their simulations generate aseismic slip pulses that propagate in the direction of fluid flow. In their model, fluid pressurization causes weakening, which induces slip acceleration that, in turn, increases permeability by a few orders of magnitude. This is consistent with our inferences in that the occurrence of slow slip requires high permeability. In addition, in regions where slow slip occurs, they find a negative correlation between slip rate and effective normal stress, indicating that fault strength plays a significant role even in more complex models. In line with our results and Perez-Silva et al. (2023), slow slip arises in both velocity-weakening and velocity-strengthening faults, although it is unclear from their model whether this mechanism is more efficient in either frictional condition.

Other models have coupled fluid flow with the poroelastic response or the evolution of porosity to generate slow slip in velocity-weakening faults. Marguin and Simpson (2023) investigated the coupled role of fluid overpressure and permeability evolution on fault slip. The model consisted of a velocity-weakening fault embedded in a poro-elastic medium overlying a poro-viscoelastic substrate. Their results show that both changes in effective stress and permeability variations influence fault slip behavior, particularly the characteristics of earthquake sequences. In this framework, SSEs precede earthquakes in models that account for the full pore-elastic coupling, as the pore-pressure reduction during initial rupture propagation stabilizes slip (Marguin & Simpson, 2023). Following a different approach, Yang and Dunham (2021) modeled the effects of compaction and dilation on earthquakes and slow slip sequences. In this model, SSEs do not arise as a result of permeability changes, which are quite small, but are instead driven by pressurization due to compaction and velocity-weakening friction, while slip accelerations are quenched by pore-pressure reduction driven by suction during dilatancy.

Together, these models highlight that fluid flow combined with different hydromechanical processes—including permeability evolution (through slip, time and effective stress), porosity evolution (through dilatancy and compaction), poro-elasticity—may play an important role in slow slip generation. More research into slow slip environments and the hydraulic properties of the fault zone is needed to determine the relative contributions of these mechanisms to slow slip generation.

7. Conclusions

We impose periodic pore-pressure perturbations on a mildly velocity-weakening fault region. To model pore-pressure changes, we consider a one-way coupling, in which fault slip is related to pore-pressure changes through changes in effective normal stress. We assume that fluids are injected at the center of the fault and diffuse along the fault plane following the axisymmetric diffusion equation. Our results indicate that these perturbations induce a range of fault slip behaviors, including slow slip events (SSEs). These induced SSEs have properties that range from ∼3 months to over 3 years and M_w 5.5 − 7.5. However, the model fails to capture the broad range of SSE properties observed in subduction zones. In addition, the range of induced SSE properties is narrower than that for velocity-strengthening fault regions (Perez-Silva et al., 2023). Our model indicates that large hydraulic diffusivities ($1\ m^2/s < D < 100\ m^2/s$) are required to generate SSEs in velocity-weakening regions, which corresponds to permeabilities ranging from 5×10^{-12} to $5 \times 10^{-10}\ m^2$. These large permeabilities can be attributed to transient increases in fault zone properties during SSEs, which have been inferred from field observations. Further constraints on hydraulic properties at SSE depths are required to test the model predictions.

Conflict of Interest

The authors declare no conflicts of interest relevant to this study.

Availability Statement

The numerical data used to produce the figures is available at Zenodo via Perez-Silva et al. (2026).

Acknowledgments
We thank Martha Savage, Emily Warren-Smith and Laura Wallace for fruitful discussion on the initial modeling approach. We also thank Betti Hegyi and an anonymous reviewer for their constructive comments, which allowed us to improve the quality of the manuscript. A.P-S. and T.W. are funded by MBIE Endeavour Fund (Smart Ideas, Grant UOOX2206). This work was supported by JSPS KAKENHI (21H05206) and JST FOREST Program (JPMJFR241C). Computing resources were provided by the New Zealand eScience Infrastructure (NeSI) high-performance computing facilities. Open access publishing facilitated by University of Otago, as part of the Wiley - University of Otago agreement via the Council of Australasian University Librarians.

References

Audet, P., Bostock, M. G., Christensen, N. I., & Peacock, S. M. (2009). Seismic evidence for overpressured subducted oceanic crust and megathrust fault sealing. *Nature*, *457*(7225), 76–78. https://doi.org/10.1038/nature07650

Behr, W. M., & Bürgmann, R. (2021). What's down there? The structures, materials and environment of deep-seated slow slip and tremor. *Philosophical Transactions of the Royal Society A: Mathematical, Physical and Engineering Sciences*, *379*(2193), 20200218. https://doi.org/10.1098/rsta.2020.0218

Condit, C. B., & French, M. E. (2022). Geologic evidence of lithostatic pore fluid pressures at the base of the subduction seismogenic zone. *Geophysical Research Letters*, *49*(12), e2022GL098862. https://doi.org/10.1029/2022GL098862

Cruz-Atienza, V. M., Villafuerte, C., & Bhat, H. S. (2018). Rapid tremor migration and pore-pressure waves in subduction zones. *Nature Communications*, *9*(1), 2900. https://doi.org/10.1038/s41467-018-05150-3

Dieterich, J. H. (1979). Modeling of rock friction: 1. Experimental results and constitutive equations. *Journal of Geophysical Research*, *84*(B5), 2161–2168. https://doi.org/10.1029/JB084iB05p02161

Farge, G., Jaupart, C., & Shapiro, N. M. (2021). Episodicity and migration of low frequency earthquakes modeled with fast fluid pressure transients in the permeable subduction interface. *Journal of Geophysical Research: Solid Earth*, *126*(9), e2021JB021894. https://doi.org/10.1029/2021JB021894

Frank, W. B., Shapiro, N. M., Husker, A. L., Kostoglodov, V., Bhat, H. S., & Campillo, M. (2015). Along-fault pore-pressure evolution during a slow-slip event in Guerrero, Mexico. *Earth and Planetary Science Letters*, *413*, 135–143. https://doi.org/10.1016/j.epsl.2014.12.051

Ganzhorn, A., Pilorgé, H., & Reynard, B. (2019). Porosity of metamorphic rocks and fluid migration within subduction interfaces. *Earth and Planetary Science Letters*, *522*, 107–117. https://doi.org/10.1016/j.epsl.2019.06.030

Gao, H., Schmidt, D. A., & Weldon, R. J. (2012). Scaling relationships of source parameters for slow slip events. *Bulletin of the Seismological Society of America*, *102*(1), 352–360. https://doi.org/10.1785/0120110096

Gosselin, J. M., Audet, P., Estève, C., McLellan, M., Mosher, S. G., & Schaeffer, A. J. (2020). Seismic evidence for megathrust fault-valve behavior during episodic tremor and slip. *Science Advances*, *6*(4), eaay5174. https://doi.org/10.1126/sciadv.aay5174

Heimisson, E. R., Dunham, E. M., & Almquist, M. (2019). Poroelastic effects destabilize mildly rate-strengthening friction to generate stable slow slip pulses. *Journal of the Mechanics and Physics of Solids*, *130*, 262–279. https://doi.org/10.1016/j.jmps.2019.06.007

Herath, P., & Audet, P. (2024). Fluid upwelling across the Hikurangi subduction thrust during deep slow-slip earthquakes. *Communications Earth & Environment*, *5*(1), 697. https://doi.org/10.1038/s43247-024-01864-z

Hong, T., & Marone, C. (2005). Effects of normal stress perturbations on the frictional properties of simulated faults. *Geochemistry, Geophysics, Geosystems*, *6*(3), Q03012. https://doi.org/10.1029/2004GC000821

Hosseini, N., Paluszny, A., & Zimmerman, R. W. (2025). Dynamics of fluid-driven slip on a 3D heterogeneous fault with rate-and-state friction. *Journal of Geophysical Research: Solid Earth*, *130*(7), e2025JB031221. https://doi.org/10.1029/2025JB031221

Ikari, M. J., Wallace, L. M., Rabinowitz, H. S., Savage, H. M., Hamling, I. J., & Kopf, A. J. (2020). Observations of laboratory and natural slow slip events: Hikurangi subduction zone, New Zealand. *Geochemistry, Geophysics, Geosystems*, *21*(2), e2019GC008717. https://doi.org/10.1029/2019GC008717

Kaneko, Y., Avouac, J.-P., & Lapusta, N. (2010). Towards inferring earthquake patterns from geodetic observations of interseismic coupling. *Nature Geoscience*, *3*(5), 363–369. https://doi.org/10.1038/ngeo843

Katayama, I., Terada, T., Okazaki, K., & Tanikawa, W. (2012). Episodic tremor and slow slip potentially linked to permeability contrasts at the Moho. *Nature Geoscience*, *5*(10), 731–734. https://doi.org/10.1038/ngeo1559

Kawano, S., Katayama, I., & Okazaki, K. (2011). Permeability anisotropy of serpentinite and fluid pathways in a subduction zone. *Geology*, *39*(10), 939–942. https://doi.org/10.1130/G32173.1

Kita, S., Houston, H., Yabe, S., Tanaka, S., Asano, Y., Shibutani, T., & Suda, N. (2021). Effects of episodic slow slip on seismicity and stress near a subduction-zone megathrust. *Nature Communications*, *12*(1), 7253. https://doi.org/10.1038/s41467-021-27453-8

Lapusta, N., & Liu, Y. (2009). Three-dimensional boundary integral modeling of spontaneous earthquake sequences and aseismic slip. *Journal of Geophysical Research*, *114*(B9), B09303. https://doi.org/10.1029/2008JB005934

Linker, M., & Dieterich, J. H. (1992). Effects of variable normal stress on rock friction: Observations and constitutive equations. *Journal of Geophysical Research*, *97*(B4), 4923–4940. https://doi.org/10.1029/92JB00017

Liu, Y., & Rice, J. R. (2005). Aseismic slip transients emerge spontaneously in three-dimensional rate and state modeling of subduction earthquake sequences. *Journal of Geophysical Research*, *110*(B8), B08307. https://doi.org/10.1029/2004JB003424

Liu, Y., & Rice, J. R. (2007). Spontaneous and triggered aseismic deformation transients in a subduction fault model. *Journal of Geophysical Research*, *112*, B09404. https://doi.org/10.1029/2007JB004930.f

Marguin, V., & Simpson, G. (2023). Influence of fluids on earthquakes based on numerical modeling. *Journal of Geophysical Research: Solid Earth*, *128*(2), e2022JB025132. https://doi.org/10.1029/2022JB025132

Marone, C. (1998). Laboratory-derived friction laws and their application to seismic faulting. *Annual Review of Earth and Planetary Sciences*, *26*(1), 643–696. https://doi.org/10.1146/annurev.earth.26.1.643

Muñoz-Montecinos, J., & Behr, W. M. (2023). Transient permeability of a deep-seated subduction interface shear zone. *Geophysical Research Letters*, *50*(20), e2023GL104244. https://doi.org/10.1029/2023GL104244

Nakajima, J., & Uchida, N. (2018). Repeated drainage from megathrusts during episodic slow slip. *Nature Geoscience*, *11*(5), 351–356. https://doi.org/10.1038/s41561-018-0090-z

Noda, H., Lapusta, N., & Kanamori, H. (2013). Comparison of average stress drop measures for ruptures with heterogeneous stress change and implications for earthquake physics. *Geophysical Journal International*, *193*(3), 1691–1712. https://doi.org/10.1093/gji/ggt074

Oncken, O., Angiboust, S., & Dresen, G. (2022). Slow slip in subduction zones: Reconciling deformation fabrics with instrumental observations and laboratory results. *Geosphere*, *18*(1), 104–129. https://doi.org/10.1130/GES02382.1

Ozawa, S., Yang, Y., & Dunham, E. M. (2024). Fault-valve instability: A mechanism for slow slip events. *Journal of Geophysical Research: Solid Earth*, *129*(10), e2024JB029165. https://doi.org/10.1029/2024JB029165

Peacock, S. M., Christensen, N. I., Bostock, M. G., & Audet, P. (2011). High pore pressures and porosity at 35 km depth in the Cascadia subduction zone. *Geology*, *39*(5), 471–474. https://doi.org/10.1130/G31649.1

Perez-Silva, A., Kaneko, Y., Savage, M., Wallace, L., & Warren-Smith, E. (2023). Characteristics of slow slip events explained by rate-strengthening faults subject to periodic pore fluid pressure changes. *Journal of Geophysical Research: Solid Earth*, *128*(6), e2022JB026332. https://doi.org/10.1029/2022JB026332

Perez-Silva, A., Kaneko, Y., & Wang, T. (2026). Pore-pressure cycles and slow slip generation on mildly velocity-weakening faults [Dataset]. *Zenodo*. https://doi.org/10.1038/s41561-018-0090-z

Perez-Silva, A., Li, D., Gabriel, A.-A., & Kaneko, Y. (2021). 3D Modeling of long-term slow slip events along the flat-slab segment in the Guerrero Seismic Gap, Mexico. *Geophysical Research Letters*, *48*(13), e2021GL092968. https://doi.org/10.1029/2021GL092968

Perfettini, H., & Ampuero, J.-P. (2008). Dynamics of a velocity strengthening fault region: Implications for slow earthquakes and postseismic slip. *Journal of Geophysical Research*, *113*(B9), B09411. https://doi.org/10.1029/2007JB005398

Rabinowitz, H., Savage, H., Skarbek, R., Ikari, M. J., Carpenter, B. M., & Collettini, C. (2018). Frictional behavior of input sediments to the Hikurangi Trench, New Zealand. *Geochemistry, Geophysics, Geosystems*, *19*(9), 2973–2990. https://doi.org/10.1029/2018GC007633

Rice, J. R., & Ruina, A. L. (1983). Stability of steady frictional slipping. *Journal of Applied Mechanics*, *50*(2), 343–349. https://doi.org/10.1115/1.3167042

Richardson, E., & Marone, C. (1999). Effects of normal stress vibrations on frictional healing. *Journal of Geophysical Research*, *104*(B12), 28859–28878. https://doi.org/10.1029/1999JB900320

Rubin, A. M. (2008). Episodic slow slip events and rate-and-state friction. *Journal of Geophysical Research*, *113*(B11), B11414. https://doi.org/10.1029/2008JB005642

Rubin, A. M., & Ampuero, J.-P. (2005). Earthquake nucleation on (aging) rate and state faults. *Journal of Geophysical Research*, *110*(B11), B11312. https://doi.org/10.1029/2005JB003686

Sáez, A., Lecampion, B., Bhattacharya, P., & Viesca, R. C. (2022). Three-dimensional fluid-driven stable frictional ruptures. *Journal of the Mechanics and Physics of Solids*, *160*, 104754. https://doi.org/10.1016/j.jmps.2021.104754

Saffer, D. M., & Tobin, H. J. (2011). Hydrogeology and mechanics of subduction zone forearcs: Fluid flow and pore pressure. *Annual Review of Earth and Planetary Sciences*, *39*(1), 157–186. https://doi.org/10.1146/annurev-earth-040610-133408

Segall, P., Rubin, A. M., Bradley, A. M., & Rice, J. R. (2010). Dilatant strengthening as a mechanism for slow slip events. *Journal of Geophysical Research*, *115*(B12), B12305. https://doi.org/10.1029/2010JB007449

Shibazaki, B., & Iio, Y. (2003). On the physical mechanism of silent slip events along the deeper part of the seismogenic zone. *Geophysical Research Letters*, *30*(9), 1489. https://doi.org/10.1029/2003GL017047

Shreedharan, S., Rivière, J., Bhattacharya, P., & Marone, C. (2019). Frictional state evolution during normal stress perturbations probed with ultrasonic waves. *Journal of Geophysical Research: Solid Earth*, *124*(6), 5469–5491. https://doi.org/10.1029/2018JB016885

Sibson, R. (1992). Implications of fault-valve behaviour for rupture nucleation and recurrence. *Tectonophysics*, *211*(1–4), 283–293. https://doi.org/10.1016/0040-1951(92)90065-E

Skarbek, R. M., & Saffer, D. M. (2009). Pore pressure development beneath the décollement at the Nankai subduction zone: Implications for plate boundary fault strength and sediment dewatering. *Journal of Geophysical Research*, *114*(B7), B07401. https://doi.org/10.1029/2008JB006205

Wallace, L. M. (2020). Slow slip events in New Zealand. *Annual Review of Earth and Planetary Sciences*, *48*(1), 175–203. https://doi.org/10.1146/annurev-earth-071719-055104

Wallace, L. M., & Beavan, J. (2010). Diverse slow slip behavior at the Hikurangi subduction margin, New Zealand. *Journal of Geophysical Research*, *115*(B12), B12402. https://doi.org/10.1029/2010JB007717

Wallace, L. M., Webb, S. C., Ito, Y., Mochizuki, K., Hino, R., Henrys, S., et al. (2016). Slow slip near the trench at the Hikurangi subduction zone, New Zealand. *Science*, *352*(6286), 701–704. https://doi.org/10.1126/science.aaf2349

Warren-Smith, E., Fry, B., Wallace, L., Chon, E., Henrys, S., Sheehan, A., et al. (2019). Episodic stress and fluid pressure cycling in subducting oceanic crust during slow slip. *Nature Geoscience*, *12*(6), 475–481. https://doi.org/10.1038/s41561-019-0367-x

Wech, A. G., & Bartlow, N. M. (2014). Slip rate and tremor genesis in Cascadia. *Geophysical Research Letters*, *41*(2), 392–398. https://doi.org/10.1002/2013GL058607

Xue, L., Li, H.-B., Brodsky, E. E., Xu, Z.-Q., Kano, Y., Wang, H., et al. (2013). Continuous permeability measurements record healing inside the Wenchuan earthquake fault zone. *Science*, *340*(6140), 1555–1559. https://doi.org/10.1126/science.1237237

Yang, Y., & Dunham, E. M. (2021). Effect of porosity and permeability evolution on injection-induced aseismic slip. *Journal of Geophysical Research: Solid Earth*, *126*(7), e2020JB021258. https://doi.org/10.1029/2020JB021258

Yang, Y., & Dunham, E. M. (2023). Influence of creep compaction and dilatancy on earthquake sequences and slow slip. *Journal of Geophysical Research: Solid Earth*, *128*(4), e2022JB025969. https://doi.org/10.1029/2022JB025969

Zal, H. J., Jacobs, K., Savage, M. K., Yarce, J., Mroczek, S., Graham, K., et al. (2020). Temporal and spatial variations in seismic anisotropy and V_P/V_S ratios in a region of slow slip. *Earth and Planetary Science Letters*, *532*, 115970. https://doi.org/10.1016/j.epsl.2019.115970

Zhu, W., Allison, K. L., Dunham, E. M., & Yang, Y. (2020). Fault valving and pore pressure evolution in simulations of earthquake sequences and aseismic slip. *Nature Communications*, *11*(1), 4833. https://doi.org/10.1038/s41467-020-18598-z
Zilio, L. D., & Gerya, T. (2022). Subduction earthquake cycles controlled by episodic fluid pressure cycling. *Lithos*, 426–427. https://doi.org/10.1016/j.lithos.2022.106800

References From the Supporting Information

Arnulf, A. F., Biemiller, J., Lavier, L., Wallace, L. M., Bassett, D., Henrys, S., et al. (2021). Physical conditions and frictional properties in the source region of a slow-slip event. *Nature Geoscience*, *14*(5), 334–340. https://doi.org/10.1038/s41561-021-00741-0
Carslaw, H., & Jaeger, J. (1959). *Conduction of heat in solids*. Clarendon Press.
Cheng, A. H.-D. (2016). *Poroelasticity* (Vol. 27). Springer International Publishing. https://doi.org/10.1007/978-3-319-25202-5
Mase, C. W., & Smith, L. (1987). Effects of frictional heating on the thermal, hydrologic, and mechanical response of a fault. *Journal of Geophysical Research*, *92*(B7), 6249–6272. https://doi.org/10.1029/JB092iB07p06249
Rice, J. R. (2006). Heating and weakening of faults during earthquake slip. *Journal of Geophysical Research*, *111*(B5), B05311. https://doi.org/10.1029/2005JB004006
Segall, P., & Rice, J. R. (1995). Dilatancy, compaction, and slip instability of a fluid-infiltrated fault. *Journal of Geophysical Research*, *100*(B11), 22155–22171. https://doi.org/10.1029/95JB02403
Stehfest, H. (1970). Numerical inversion of Laplace transforms. *Communications of the ACM*, *13*(1), 47–49. https://doi.org/10.1145/361953.361969
Wallace, L. M., Beavan, J., McCaffrey, R., & Darby, D. (2004). Subduction zone coupling and tectonic block rotations in the North Island, New Zealand. *Journal of Geophysical Research*, *109*(B12), B12406. https://doi.org/10.1029/2004JB003241
Wibberley, C. A. J. (2002). Hydraulic diffusivity of fault gouge zones and implications for thermal pressurization during seismic slip. *Earth, Planets and Space*, *54*(11), 1153–1171. https://doi.org/10.1186/BF03353317

Supporting Information for "Pore-pressure Cycles and Slow Slip Generation on Mildly Velocity-Weakening Faults"

Andrea Perez-Silva[1,2], Yoshihiro Kaneko[3], Ting Wang[1]

[1]University of Otago, Dunedin, New Zealand

[2]Now at GFZ Helmholtz Centre for Geosciences, Potsdam, Germany

[3]Kyoto University, Department of Geophysics, Graduate School of Science, Kyoto, Japan

Contents of this file

Text S1: Model parameters

Our model consists of a circular velocity-weakening (VW) patch surrounded by velocity-strengthening (VS) friction properties (Figure 1b). The VS region has a constant $a - b = 0.001$ with $a = 0.015$ and $b = 0.014$ for all cases. For the VW patch, we consider mildly VW friction with $a - b = -0.001$ to -0.002, and a/b decreasing linearly from 0.94 to 0.81. The radius of the VW patch ranges from 15 to 60 km, which is comparable to the size of SSE patches along the Hikurangi margin (Wallace & Beavan, 2010; Wallace, 2020).

The shear modulus μ is set to 10 GPa, which is within the range estimated along the shallow Hikurangi margin (6 – 14 GPa, Arnulf et al., 2021). The effective normal stress σ is set to 3 MPa, such a low value is set to reduce computational costs. We set the plate convergence rate to 50 mm/yr, consistent with the plate rate in the central to northern North Island of New Zealand, where frequent SSEs occur offshore Gisborne (Wallace et al., 2004).

Previous numerical models have shown that the fault slip behavior in VW faults depends on the effective fault stiffness ratio W/h^*, where W is the width of the VW region (Liu & Rice, 2007). Large values of W/h^* lead to earthquakes, while for cases where the ratio is close to unity, SSEs emerge (Liu & Rice, 2007). In our study, the fault stiffness ratio is given by $2R/h^*_{RR}$.

Text S2: Modeling of pore-pressure perturbations

We model pore-pressure perturbations on the fault following the Type II perturbation described in Perez-Silva et al. (2023). Fluid is injected at a constant rate q_0 (in m/s) and diffuses along the fault plane following the axisymmetric fluid diffusion equation:

$$\frac{\partial p_{\mathrm{f}}(r,t)}{\partial t} = D\left(\frac{\partial^2 p_{\mathrm{f}}(r,t)}{\partial r^2} + \frac{1}{r}\frac{\partial p_{\mathrm{f}}(r,t)}{\partial r}\right) \tag{1}$$

where r is the radial distance in km and D is the hydraulic diffusivity in m^2/s, which we assume is uniform over the fault plane. In the time domain, the solution of Equation S1 can be expressed in the following functional form (eq. 7.647, Cheng, 2016):

$$p_{\mathrm{f}}(r,t) = \frac{q_0 r_0}{\kappa}\,\Pi(r,t) \tag{2}$$

where κ is the permeability or mobility coefficient (i.e., permeability divided by dynamic viscosity) in $\mathrm{m}^2/\mathrm{Pa{\cdot}s}$ and Π is the dimensionless pore-pressure evolution, given by (section 13.5, eq. 17, Carslaw & Jaeger, 1959):

$$\Pi(r,t) = -\frac{2}{\pi r_0}\int_0^\infty \left(1 - e^{-Du^2 t}\right)\frac{J_0(ur)Y_1(ur_0) - Y_0(ur)J_1(ur_0)}{u^2[J_1^2(ur_0) + Y_1^2(ur_0)]}du \tag{3}$$

where J_i and Y_i are respectively the Bessel functions of the first and second kind of order i, with $i = 0$ or 1. Note that the factor $1/r_0$ in Equation S3 is included in the errata of eq. 7.647 in Cheng (2016). To model the pore-pressure perturbation, we use the exact solution of Equation S3 solved via numerical inversion of the Laplace transform (Stehfest, 1970; Cheng, 2016), where Equation S3 is valid for $r \geq r_0$. The evolution of pore-pressure during the perturbation is given by:

$$\Delta p_{\mathrm{f}}(r,t^*) = \frac{q_0 r_0}{\kappa}\left[\Pi(r,Dt^*)H(t^*) - \Pi(r,D_b(t^* - t_{\mathrm{inj}}))H(t^* - t_{\mathrm{inj}})\right], \tag{4}$$

where t_{inj} is the time over which fluids flow into the fault plane, and D and D_b are the hydraulic diffusivity before t_{inj} and after t_{inj}, respectively.

The normalized perturbation size and amplitude correspond to $\sqrt{Dt_{\mathrm{inj}}}/r_0$ and $\Delta p_{\mathrm{max}}/\sigma$, respectively. The length scale r_0 could be interpreted as the width of the fluid source.

Unless otherwise noted, we assume $r_0 = 1$ km to ensure that r_0 is properly resolved by our simulations (0.35 km $< \Delta x <$ 0.82 km, Table 1 in the main text). Note that, since Equation S3 is valid for $r \geq r_0$, we simply assume a constant value $\Delta p_\mathrm{f}(r_0, t^*)$ within $0 < r < r_0$.

Text S3: Description of additional slip behaviors

Induced SSEs followed by spontaneous SSEs

Based on the analysis of the perturbation period T_per (Figure 3), a distinct pattern emerges in the fault response for long T_per: Induced SSEs are consistently followed by semi-spontaneous SSEs. These two types of SSEs are differentiated by their timing relative to the pore-pressure perturbation. Induced SSEs occur concurrently with the pore-pressure change, whereas semi-spontaneous SSEs arise later, without any ongoing perturbation. Figure S1 provides an illustration of this pattern in a simulation case with $\Delta p_\mathrm{max}/\sigma = 0.1$ and $T_\mathrm{per} = 5$ years from Figure 3b. The initial perturbation at $t = 25$ yr induces an SSE, marked by a two-order-of-magnitude increase in V_max above the plate rate, which corresponds to an induced SSE. Following this SSE, the shear strength τ gradually returns to its initial value. At the culmination of this recovery phase, the shear strength τ exceeds its original level, and the slip velocity rises above the plate rate, thus generating a semi-spontaneous SSE (Figure S1b). This last SSE is not a direct consequence of the pore-pressure change but rather the concluding stage of shear stress recovery. After the semi-spontaneous SSE, the fault returns to a steady state ($V_\mathrm{max} = V_\mathrm{pl}$) and remains there until the onset of the next perturbation at $t = 30$ years (Figure S1b). The second perturbation then initiates a similar sequence: an SSE is induced by the pore-pressure change, followed by a semi-spontaneous SSE during the subsequent shear strength recovery (Figure S1b). The detailed spatio-temporal evolution of the field variables during an induced and a semi-spontaneous SSE is depicted in Figures S1c to S1e and Figures S1f to S1h, respectively.

Induced earthquakes

For some simulation cases, the imposed perturbations induce earthquakes ($V_{\max} > 10^{-2}$ m/s). An example of induced earthquakes is shown in Figure S2, for a simulation case with $a/b = 0.94$, $D = 50$ m^2/s, $t_{\text{inj}} = 6$ months, $T_{\text{per}} = 7$ yr and $\Delta p/\sigma = 0.1$. Interestingly, while the initial perturbation at $t = 25$ years resulted in an SSE ($\text{V}_{\max} < 10^{-2}$ m/s), subsequent perturbations led to earthquakes ($\text{V}_{\max} > 10^{-2}$ m/s, Figure S2a). The temporal evolution of the field variables at a specific location $x = 0$, $z = 2$ km (Figure S2b) reveals a distinctive pattern. During the increase in pore pressure, both the slip rate and the shear stress increase, followed by a decrease in these variables once the perturbation subsides. Shear stress then slowly increases in the period between perturbations, while the slip velocity remains below the plate rate (Figure S2b).

The spatiotemporal evolution of $\Delta p_{\text{f}}/\sigma$, $\log_{10}(V/V_{\text{pl}})$, τ, and $\log_{10}\Omega$ during an induced earthquake is illustrated in Figures S2c to S2f. The slip rate evolution indicates that at the onset of the pore pressure increase, slip fronts propagate toward the center of the fault (Figure S2d), where they attain a peak slip velocity. Subsequently, the slip rate accelerates and the slipping area expands. Finally, slip fronts expand radially along the fault, and the maximum slip rate becomes concentrated at the front. During this expansion, the fault within the slipping region is at a steady state ($\log_{10}\Omega = 0$, Figure S2f). Notably, the slip fronts expand beyond the pressurized region (c.f., Figure S2c and S2d). As the pore pressure decreases, the slip rate diminishes, starting from the injection point (Figure S2d). Following the perturbation, the fault region within the perturbed area remains locked, with the slip velocity falling below the plate rate ($V < V_{\mathrm{pl}}$, Figure S2d).

Text S4: Permeability estimation

Hydraulic diffusivity values are less well constrained than fault zone permeability. Therefore, for comparison, we estimate permeability using the relation $k = D\eta\beta\phi$, where the permeability (k) depends on fluid viscosity (η), porosity (ϕ), the sum of pore and fluid compressibility (β), and the hydraulic diffusivity (D); the latter of which we take from our model input values (Figures 2 and 7). We consider the approximate order of magnitude of these parameters, where $\eta = 10^{-3}$ Pa s (Cheng, 2016), $\beta = 10^{-8}$ Pa^{-1} (within the range in Mase & Smith, 1987; Rice, 2006; Wibberley, 2002) and, for simplicity, we set $\phi = 0.05$, noting that ϕ may range from $\sim 10^{-2}$ to 10^{-1} (Peacock et al., 2011; Saffer & Tobin, 2011; Segall & Rice, 1995). The estimated permeability ranges from 5×10^{-12} to 5×10^{-10} m^2, as reported in the main text.

Text S5: Comparison of two *aging law* versions

To account for normal stress variations in the evolution of the state variable θ, the modified aging law by Linker and Dieterich (1992) includes an extra term, highlighted in red below:

$$\frac{\mathrm{d}\theta}{\mathrm{d}t} = 1 - \frac{V\theta}{D_{\mathrm{RS}}} - \frac{\alpha\,\theta}{b\,\bar{\sigma}}\frac{\mathrm{d}\bar{\sigma}}{\mathrm{d}t} \tag{5}$$

To assess the effect of this extra term on the model results, we conducted simulations with two different values of α: 0.2 and 0. The latter case with $\alpha = 0$ represents the aging law by Dieterich (1979).

To run the tests, we selected two cases from Figure 3, one with $\Delta p_{\mathrm{f}} = 0.1$ and $T_{\mathrm{per}} = 2.5$ yr, and another with $\Delta p_{\mathrm{f}} = 0.5$ and the same T_{per}. All other parameters are the same as in Figure 3 with $a/b = 0.94$ and $b = 0.016$. We selected this case because we expect the extra term to play a more important role for more mildly velocity-weakening faults ($a/b \sim 1$), as seen in Equation S8. For the case with $\Delta p_{\mathrm{f}}/\sigma = 0.1$, we found no significant difference in the evolution of θ, and the fault response remained the same for either value of α. In contrast, for the case with $\Delta p_{\mathrm{f}} = 0.5$, both the evolution of θ and the fault response were notably different for each value of α.

We show the model results for the case with $\Delta p_{\mathrm{f}} = 0.5$, and $\alpha = 0$ and 0.2 in Figure S4. For the case with $\alpha = 0.2$, the fault generates both earthquakes and aborted slip events (as in Figure 6a and Figure S3a to S3c) in response to the perturbations (Figure S4a). In contrast, for $\alpha = 0$, the fault response to the perturbations is predominantly earthquakes, which arise approximately every 5 yr, which is twice T_{per} (Figure S4c). Apart from the difference in fault behavior, there is also a notable difference in the evolution of τ and θ in each case. In Figure S4b and S4d, we show the temporal evolution of Ω, θ and τ at $x = 0$ and $z = 2$ km. When using the aging law by Dieterich (1979), θ and τ only evolve during earthquake occurrence (dashed black lines and dashed blue lines, respectively, in Figure S4c). In contrast, when accounting for the modified aging law by Linker and Dieterich (1992), both θ and τ evolve during most perturbations (Figure S4b). Particularly, θ transiently increases during each perturbation; it also decreases significantly when slip occurs abruptly, as in the case with $\alpha = 0$. In the cases when no significant slip occurs, the change in θ also induces a change in τ. Despite the differences in θ, we do not observe a large difference in the evolution of Ω (c.f., red lines in Figures S4b and S4d). Notably, a more stable slip behavior (i.e., less earthquakes in response to the perturbations) is found for the case accounting for Linker and Dieterich (1992).

These tests suggest that accounting for the modified aging law is only significant for large changes in $\Delta p_\mathrm{f}/\sigma$. Changes in pore-pressure in this framework cause a transient increase in θ, as expected from Equation S5. This increase in the state variable opposes the decrease in effective normal stress, and thus tends to strengthen the fault. We expect that the effect of α also increases with the perturbation size.

Caption for Movies S1 - S5: Movies of slip rate evolution of representative models shown in the main text. *Movie S1*: Repeating SSE (Section 4.1). *Movies S2 - S3*: Non-repeating SSE (Section 4.2). Instantaneously induced SSE (Movie S2), delayed-onset SSE (Movie S3). *Movies S4 - S5*: SSEs and earthquakes (Section 4.3). Induced earthquake (Movie S4) and induced SSE (Movie S5).

Table S1. Simulation parameters for cases that induced SSEs with duration and magnitude comparable to observed events (see Figure 7b). Note that for deep Hikurangi SSEs, we assumed $V_{\mathrm{pl}} = 40$ mm/yr (Wallace et al., 2004). Note that t_{inj} is 30 days for shallow Hikurangi SSEs and 1 year for deep Hikurangi SSEs.

Target SSEs	a/b	**R** (km)	h^*_{RR} (km)	**D** (m^2/s)	$\sqrt{Dt_{\mathrm{inj}}}/h^*_{\mathrm{RR}}$	$\Delta p_{\mathrm{max}}/\sigma$	T_{per} (yr)
Shallow Hikurangi	0.94	15	17.45	50	0.65	0.1	4.5
	0.87	15	11.12	50	1.02	0.1	4.5
	0.87	15	11.12	100	16.1	0.1	5.0
Deep Hikurangi	0.94	30	17.45	1	0.32	0.1	4.5
	0.94	45	17.45	1	0.32	0.1	5.0

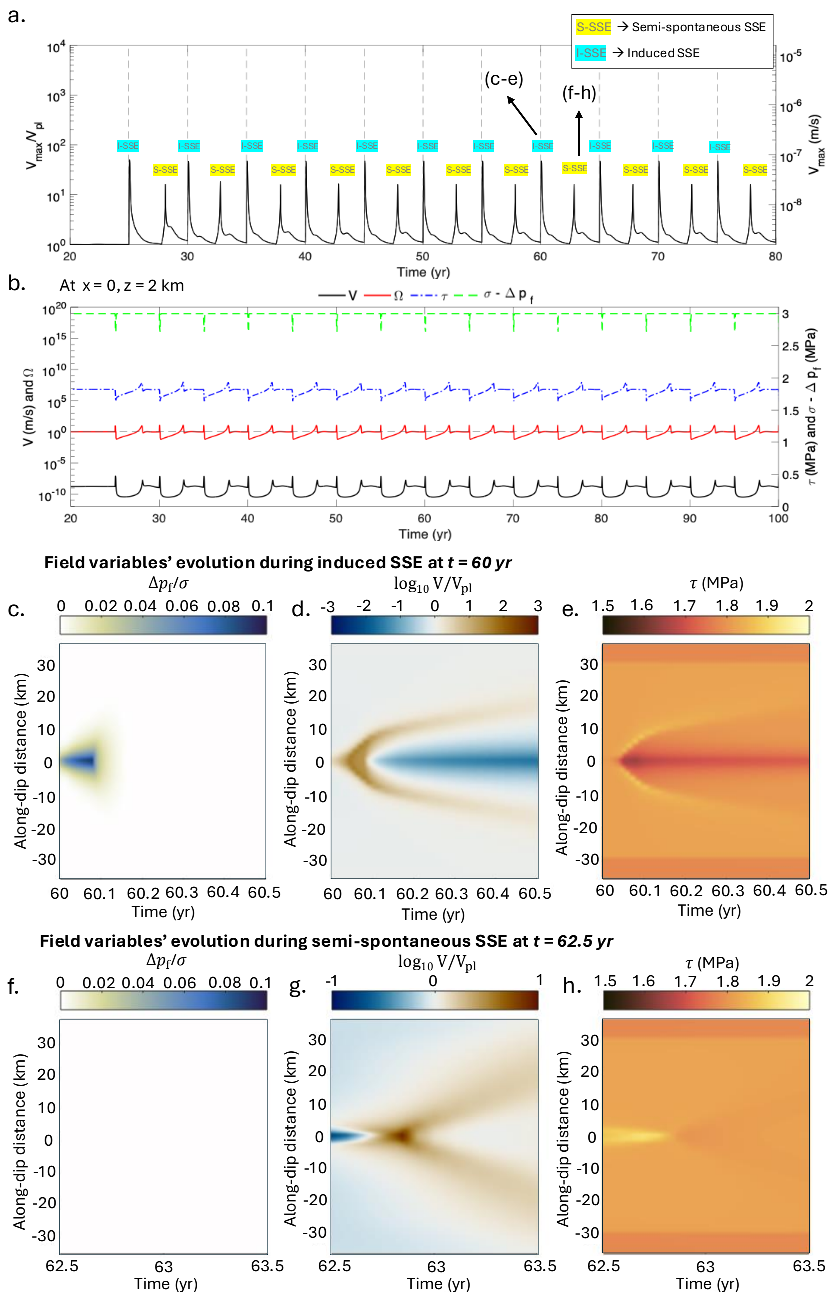

Figure S1. Example of non-repeating SSEs in a simulation with $R = 30$ km and $a/b = 0.94$; and pore-pressure perturbation parameters $D = 10\ \mathrm{m}^2/\mathrm{s}$, t_{inj}= 30 days, $\Delta p_{\mathrm{f}}/\sigma = 0.1$, and T_{per} = 2.5 years. (a) Evolution of maximum slip rate (V_{max}) over time. Vertical dashed lines mark the start time of each perturbation, with the first perturbation started at $t = 25$ years. (b) Temporal evolution of field variables slip velocity (V, solid black line), proximity to steady-state $\Omega = V\theta/D_{\mathrm{RS}}$ (solid magenta line), shear stress (τ, dashed blue line), friction coefficient (dashed red line) and effective normal stress ($\sigma - \Delta p_{\mathrm{f}}$, dashed green line) at $x = 0$ and $z = 2$ km. (c-f) Spatiotemporal evolution along depth of field variables (c-f) $\Delta p_{\mathrm{f}}/\sigma$, (d-g) $\log_{10}(V/V_{\mathrm{pl}})$ and (e-h) τ. Field variables correspond to (c-e) an induced SSE (I-SSE) and (f-h) a semi-spontaneous SSE (S-SSE).

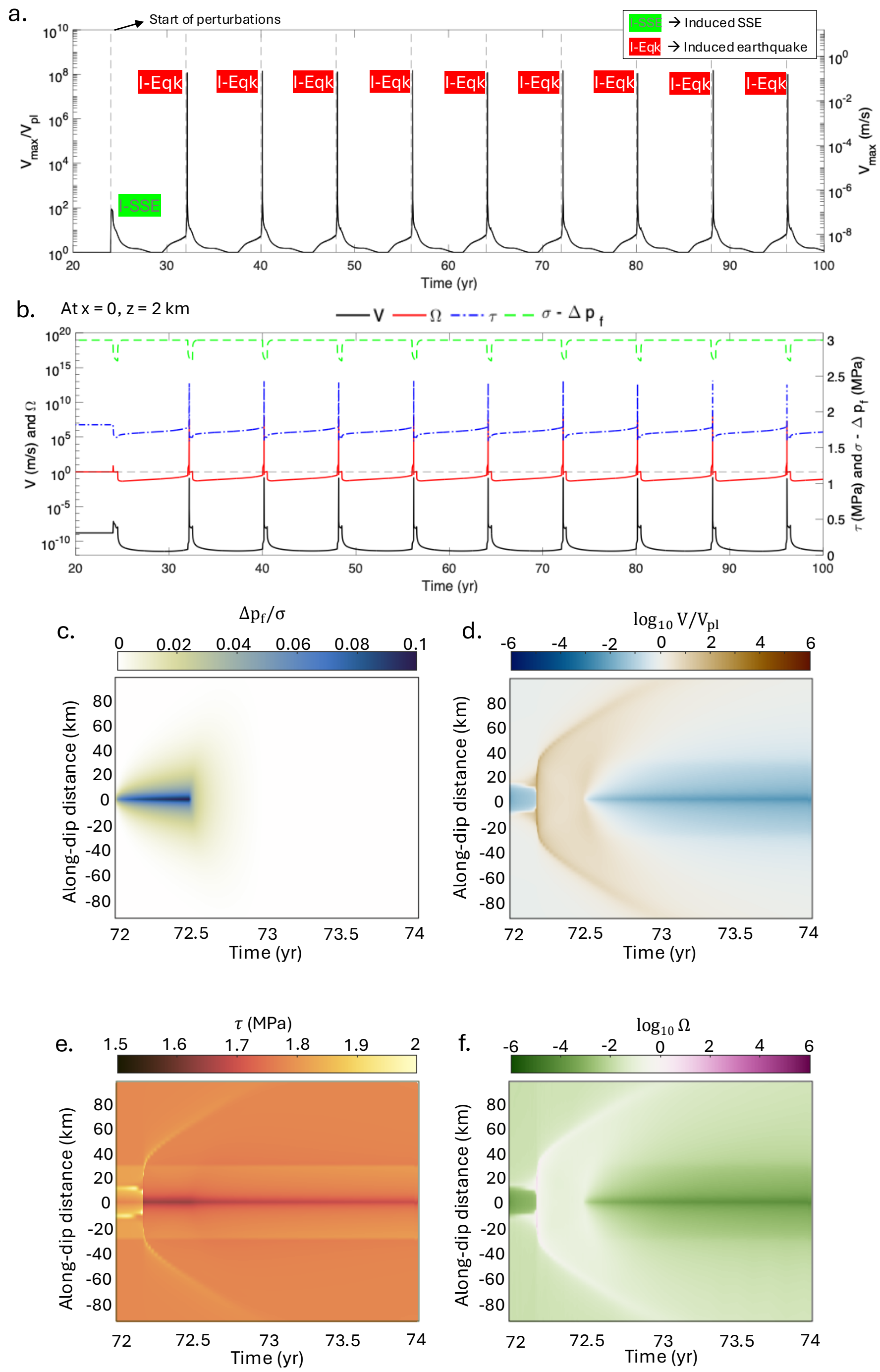

Figure S2. Example of simulation case leading to induced earthquakes. Simulation parameters: $R = 30$ km and $a/b = 0.94$; and pore-pressure perturbation parameters $D = 50$ m^2/s, $t_{\text{inj}} = 0.5$ yr, $\Delta p_{\text{f}}/\sigma = 0.1$, and $T_{\text{per}} = 7$ yr. (a) Evolution of maximum slip rate (V_{max}) over time. (b) Temporal evolution of field variables slip velocity (V, solid black line), proximity to steady-state $\Omega = V\theta/D_{\text{RS}}$ (solid magenta line), shear stress (τ, dashed blue line), friction coefficient (dashed red line) and effective normal stress ($\sigma - \Delta p_{\text{f}}$, dashed green line) at $x = 0$ and $z = 2$ km. (c-f) Spatiotemporal evolution along depth during one induced earthquake of (c) $\Delta p_{\text{f}}/\sigma$, (d) $\log_{10}(V/V_{\text{pl}})$ (e) τ and (f) $\log_{10}\Omega$. $\Omega = V\theta/D_{\text{RS}}$ measures the proximity to steady state, where $\Omega = 1$ is at steady state, $\Omega > 1$ is above steady state and $\Omega < 1$ is below steady state.

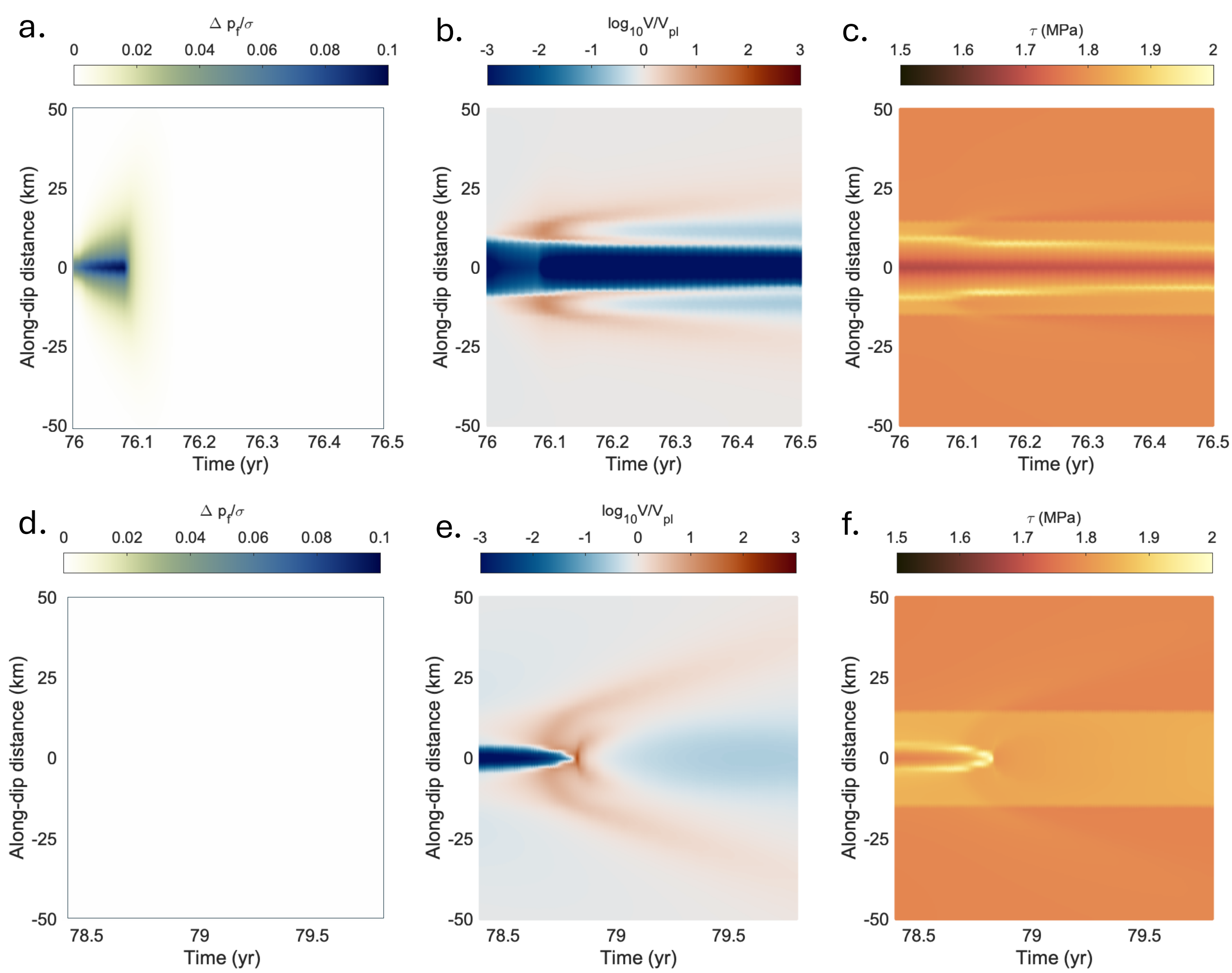

Figure S3. Evolution of field variables $\Delta p_\mathrm{f}/\sigma$, $\log_{10}(V/V_\mathrm{pl})$ and τ for simulation case shown in Figure 6 in the main text. Examples of slip behaviors showing (a-c) an aborted rupture and (d-f) a delayed-onset SSE.

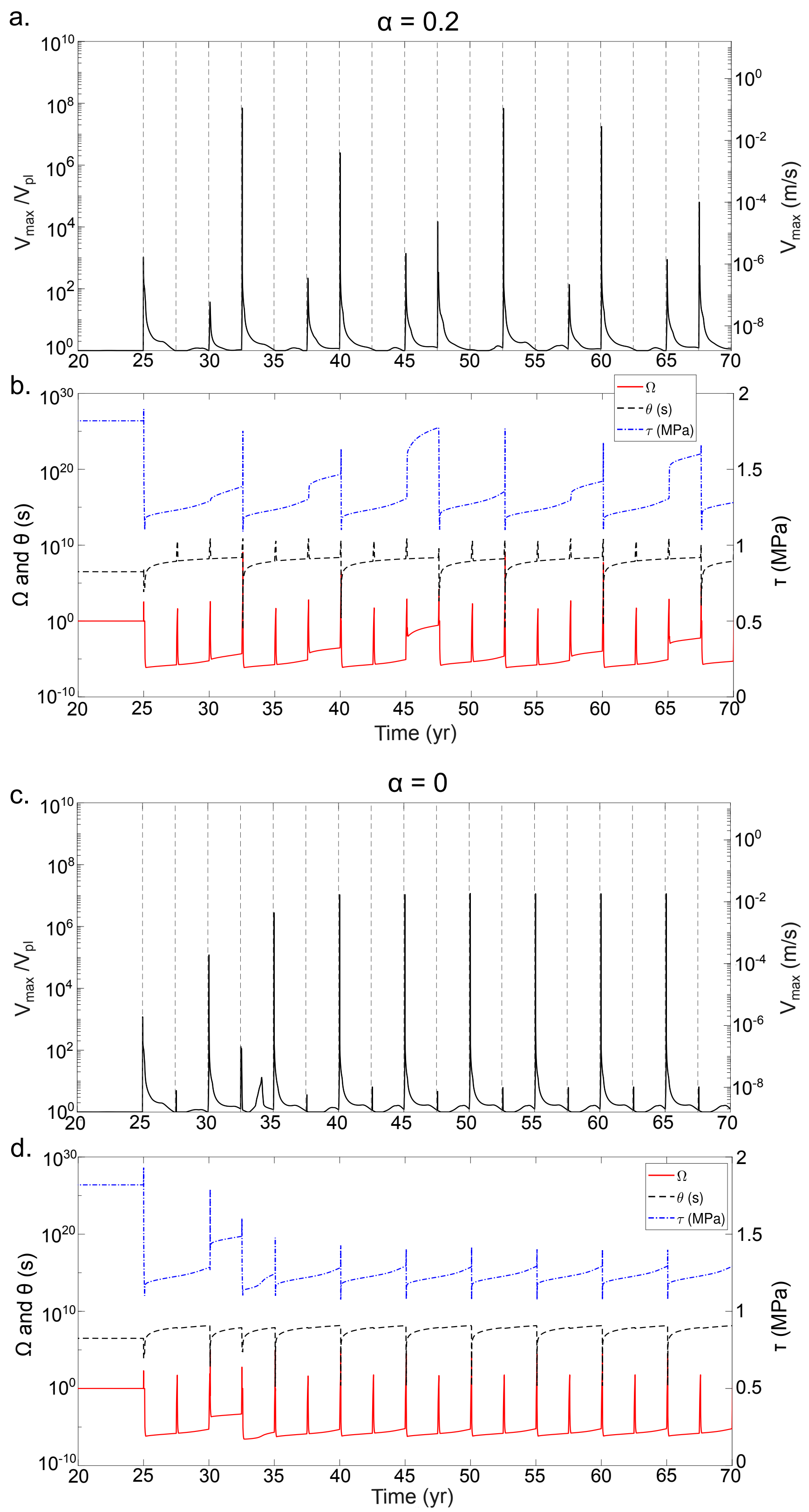

Figure S4. Comparison of model results for the same simulations case with (a-b) $\alpha = 0.2$ and (c-d) $\alpha = 0$.. Model parameters corresponds to that in Figure 3b (in the main text), with $\Delta p_{\mathrm{f}}/\sigma = 0.5$ and $T_{\mathrm{per}} = 2.5$ yr. (a-c) Evolution of V_{max}. Dashed black lines indicate the timing of the pore-pressure perturbations. (b-d) Evolution of Ω (red line), θ (dashed black line) and τ (dashed blue line).

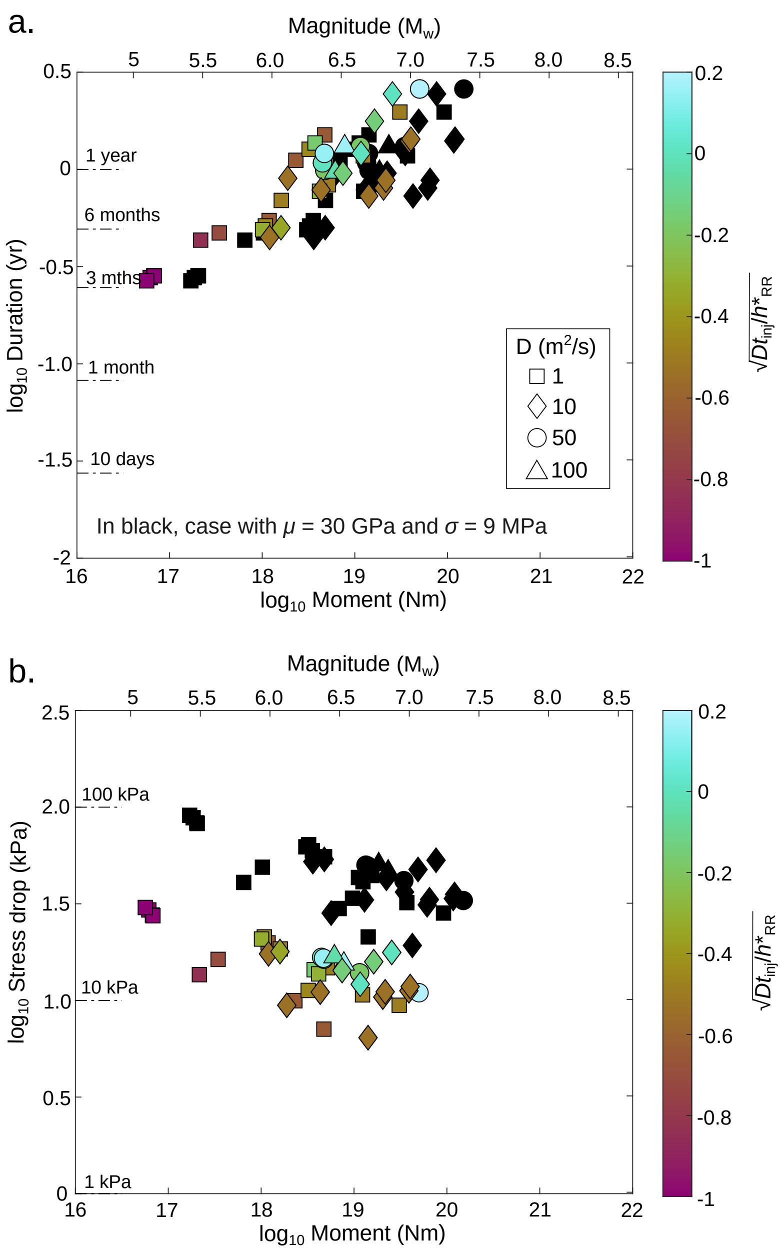

Figure S5. Comparison of SSEs properties for cases with (1) $\mu = 10$ GPa and $\sigma = 3$ MPa (in color) and (2) $\mu = 30$ GPa and $\sigma = 9$ MPa (in black). The latter case corresponds to the results presented in Figures 7a and 7b in the main text.

References

Arnulf, A. F., Biemiller, J., Lavier, L., Wallace, L. M., Bassett, D., Henrys, S., … Faverola, A. P. (2021). Physical conditions and frictional properties in the source region of a slow-slip event. *Nature Geoscience*, *14*, 334–340. doi: 10.1038/s41561-021-00741-0

Carslaw, H., & Jaeger, J. (1959). *Conduction of heat in solids.* Clarendon Press, Oxford.

Cheng, A. H.-D. (2016). *Poroelasticity* (Vol. 27). Springer International Publishing. doi: 10.1007/978-3-319-25202-5

Dieterich, J. H. (1979). Modeling of rock friction: 1. Experimental results and constitutive equations. *Journal of Geophysical Research: Solid Earth*, *84*, 2161–2168. doi: 10.1029/JB084iB05p02161

Linker, M., & Dieterich, J. H. (1992). Effects of variable normal stress on rock friction: Observations and constitutive equations. *Journal of Geophysical Research: Solid Earth*, *97*, 4923–4940. doi: 10.1029/92JB00017

Liu, Y., & Rice, J. R. (2007). Spontaneous and triggered aseismic deformation transients in a subduction fault model. *Journal of Geophysical Research: Solid Earth*, *112*, B09404. doi: 10.1029/2007JB004930.f

Mase, C. W., & Smith, L. (1987). Effects of frictional heating on the thermal, hydrologic, and mechanical response of a fault. *Journal of Geophysical Research*, *92*, 6249. doi: 10.1029/JB092iB07p06249

Peacock, S. M., Christensen, N. I., Bostock, M. G., & Audet, P. (2011). High pore pressures and porosity at 35 km depth in the Cascadia subduction zone. *Geology*, *39*, 471–474. doi: 10.1130/G31649.1

Perez-Silva, A., Kaneko, Y., Savage, M., Wallace, L., & Warren-Smith, E. (2023). Characteristics of slow slip events explained by rate-strengthening faults subject to periodic pore fluid pressure changes. *Journal of Geophysical Research: Solid Earth*, *128*(6), e2022JB026332. doi: 10.1029/2022JB026332

Rice, J. R. (2006). Heating and weakening of faults during earthquake slip. *Journal of Geophysical Research: Solid Earth*, *111*, B05311. doi: 10.1029/2005JB004006

Saffer, D. M., & Tobin, H. J. (2011). Hydrogeology and mechanics of subduction zone forearcs: Fluid flow and pore pressure. *Annual Review of Earth and Planetary Sciences*, *39*, 157-186. doi: 10.1146/annurev-earth-040610-133408

Segall, P., & Rice, J. R. (1995). Dilatancy, compaction, and slip instability of a fluid-infiltrated fault. *Journal of Geophysical Research: Solid Earth*, *100*, 22155-22171. doi: 10.1029/95JB02403

Stehfest, H. (1970). Numerical inversion of Laplace transforms. *Communications of the ACM*, *13*, 47–49.

Wallace, L. M. (2020). Slow slip events in New Zealand. *Annual Review of Earth and Planetary Sciences*, *48*, 175–203. doi: 10.1146/annurev-earth-071719-055104

Wallace, L. M., & Beavan, J. (2010). Diverse slow slip behavior at the Hikurangi subduction margin, New Zealand. *Journal of Geophysical Research: Solid Earth*, *115*, B12402. doi: 10.1029/2010JB007717

Wallace, L. M., Beavan, J., McCaffrey, R., & Darby, D. (2004). Subduction zone coupling and tectonic block rotations in the North Island, New Zealand. *Journal of Geophysical Research: Solid Earth*, *109*, B12406. doi: 10.1029/2004JB003241

Wibberley, C. A. J. (2002). Hydraulic diffusivity of fault gouge zones and implications for thermal pressurization during seismic slip. *Earth, Planets and Space*, *54*, 1153-1171. doi:

10.1186/BF03353317